Mechanisms of Low-Frequency Variability in North Atlantic Ocean Heat Transport and AMOC

Dylan Oldenburg*

School of Oceanography, University of Washington, Seattle, WA, USA

Robert C. J. Wills

Department of Atmospheric Sciences, University of Washington, Seattle, WA, USA

Kyle C. Armour

School of Oceanography and Department of Atmospheric Sciences, University of Washington, Seattle, WA, USA

LuAnne Thompson

School of Oceanography, University of Washington, Seattle, WA, USA

**Corresponding author*: Dylan Oldenburg, University of Washington, Box 357940, Seattle, WA 98195, oldend@uw.edu.

ABSTRACT

Northward ocean heat transport (OHT) plays a key role in climate and its variability. Here, we decompose OHT in the North Atlantic into modes of variability sorted by their dominant timescale by applying a low-frequency component analysis (LFCA) to output from three global climate models. The first low-frequency component (LFC), computed using this method, is an index of OHT variability that maximizes the ratio of low-frequency variance (occurring at decadal and longer timescales) to total variance. Lead-lag regressions of atmospheric and ocean variables onto the LFC timeseries illuminate the dominant mechanisms controlling low-frequency OHT variability. Anomalous northwesterly winds from eastern North America over the North Atlantic act to increase upper ocean density in the Labrador Sea region, enhancing deep convection, which later increases OHT via changes in the strength of the Atlantic Meridional Overturning Circulation (AMOC). The strengthened AMOC carries warm, salty water into the subpolar gyre, reducing convection and weakening AMOC and OHT. This mechanism, where changes in AMOC and OHT are driven primarily by changes in Labrador Sea deep convection, holds not only in models where the climatological (i.e., time-mean) deep convection is concentrated in the Labrador Sea, but also in models where the climatological deep convection is concentrated in the Greenland-Iceland-Norwegian (GIN) Seas. These results suggest that despite recent observations suggesting that the Labrador Sea plays a minor role in driving climatological AMOC, the Labrador Sea may still play an important role in driving low-frequency AMOC and OHT variability.

1. Introduction

The oceans play a major role in global climate by transporting heat from low to high latitudes (e.g., Ganachaud and Wunsch 2000). The Atlantic Ocean is of particular relevance to global climate because its meridional ocean heat transport (OHT) is northward in both hemispheres, unlike in the Pacific (e.g., Peixoto and Oort 1993), owing to the existence of a strong Atlantic Meridional Overturning Circulation (AMOC) (Ganachaud and Wunsch 2003). Both AMOC and Atlantic OHT experience robust variability at decadal and longer timescales in global climate models (e.g., Delworth and Zeng 2016). This variability in Atlantic OHT leads to major changes in North Atlantic climate (e.g., Covey and Thompson 1989). Variations in mid-latitude North Atlantic OHT are also linked to changes in OHT into the Nordic Seas that can impact Arctic sea ice cover (Mahajan et al. 2011; Day et al. 2012; Chylek et al. 2014; Yeager et al. 2015; Zhang 2015; Delworth et al. 2016; Li and Knutson 2017; Oldenburg et al. 2018).

Low-frequency variations in AMOC and OHT are closely linked to changes in North Atlantic sea-surface temperatures (SSTs) and sea-level pressure (SLP) (Bjerknes 1964; Kushnir 1994), both of which have exhibited substantial decadal and multidecadal variability in the twentieth century (e.g., Bjerknes 1964; Kushnir 1994; Schlesinger and Ramankutty 1994; Knight et al. 2005; Delworth et al. 2007; Ting et al. 2009; Deser et al. 2010). The North Atlantic Oscillation (NAO) appears to play a key role in driving these AMOC and SST fluctuations via surface-buoyancy-flux and wind-stress changes (Eden and Jung 2001; Mecking et al. 2015; Delworth et al. 2016; Delworth and Zeng 2016; Kim et al. 2018, 2020). Delworth and Zeng (2016) use a series of model experiments to show that NAO-linked anomalous heat fluxes in the subpolar gyre can drive cooling that results in increased upper ocean density in that region, increasing mixed-layer depths and deep-water formation, resulting in strengthened AMOC and associated OHT.

Low-frequency Atlantic OHT variability has been widely analyzed using a principal component (PC) analysis applied to low-pass filtered model output (Dong and Sutton 2001, 2002, 2003, 2005), where low-frequency variability is defined as variability at decadal and longer timescales. These analyses suggest that AMOC variability controls low-frequency OHT variability. Analyses of different low-frequency AMOC indices, such as the first PC of the low-pass filtered MOC or a convective index, all show that density anomalies in high-latitude deep-convection regions precede changes in AMOC on these timescales (Delworth et al. 1993; Danabasoglu et al. 2012b; Tulloch and Marshall 2012).

AMOC and its associated OHT are closely linked to the amount of water-mass transformation (WMT) in the high-latitude regions of the North Atlantic (Marsh 2000; Isachsen et al. 2007; Grist et al. 2009; Josey et al. 2009; Langehaug et al. 2012b). The WMT is the conversion of a parcel from one density class to another via air-sea exchanges or mixing, and is typically described as a density flux. Surface-forced WMT can be estimated from air-sea heat and freshwater fluxes (Walin 1982; Tziperman 1986; Speer and Tziperman 1992). Areas with large WMT coincide with deep mixed layers. In the North Atlantic, WMT occurs when the North Atlantic Current carries subtropical water northward, where it is cooled by air-sea fluxes, thereby becoming more dense and transforming into Subpolar Mode Water, which is the dominant water mass in the eastern subpolar region above the permanent pycnocline (Pérez-Brunius et al. 2004; McCartney and Talley 1982; Brambilla and Talley 2008).

Although there is a well-established link between AMOC and high-latitude WMT, there is debate about which high-latitude deep-water formation regions control AMOC. Recent observational analyses suggest that the Greenland-Iceland-Norwegian (GIN) Seas play a primary role, rather than the Labrador Sea (Chafik and Rossby 2019; Lozier et al. 2019; Zou et al. 2020). Global climate models (GCMs) differ in their representations of which North Atlantic deep convection regions control AMOC, partially due to temperature and salinity biases in the subpolar regions relative to observations (Langehaug et al. 2012b; Menary et al. 2015b). Several models from the Coupled Model Intercomparison Project phase 5 (CMIP5, Taylor et al. 2012), such as NCAR's Community Climate System Model version 4 (CCSM4; Gent et al. 2011), show convection primarily occurring in the Labrador Sea (Danabasoglu et al. 2012b; Brodeau and Koenigk 2016). However, others, such as the Geophysical Fluid Dynamics Laboratory Earth System Model version 2M (GFDL ESM2M; Dunne et al. 2012, 2013) and the Hadley Centre Global Environment Model version 3.1 (HadGEM3-GC3.1-LL; Roberts et al. 2019), show deep convection occurring in both the GIN Seas and the Labrador Sea. Though there has been much attention paid to which deep convection regions control climatological AMOC, a key unanswered question is whether the same regions also control low-frequency variability in AMOC and OHT.

There are two potential limitations of previous analyses of the causes of low-frequency variability in OHT. First, AMOC does not account for all of the low-frequency variability in Atlantic OHT, as it misses contributions from gyre circulation changes in response to surface wind and buoyancy flux anomalies (e.g., Eden and Jung 2001; Drijfhout and Hazeleger 2006; Menary et al. 2015a; Wills et al. 2019a). Thus, methods that composite OHT on AMOC or convective indices may be missing key contributions to low-frequency OHT variability. Second, using a PC analysis of low-pass filtered data results in a loss of temporal resolution, making it difficult to discern lead-lag relationships between variables on timescales less than the filtering period (Cane et al. 2017; Wills et al. 2019a). Here, we instead use a low-frequency component analysis (LFCA) applied directly to OHT. This method separates low-frequency from high-frequency variability based on differences in their latitudinal structure, while still retaining information about the high-frequency variability. LFCA is described in Wills et al. (2018) and has been applied to characterize modes of low-frequency Atlantic and Pacific SST variability (Wills et al. 2019a,b). LFCA makes no *a priori* assumptions about which processes drive or contribute to OHT variability. Moreover, because the resulting indices of low-frequency variability are not low-pass filtered, it is possible to discern how high-frequency variations (e.g., in SLP and surface buoyancy fluxes) contribute to OHT variations at longer timescales.

Here, we use LFCA to determine which mechanisms are responsible for the decadal to multi-decadal variability of Atlantic OHT. Specifically, we examine the role of AMOC and whether that role differs between models with different primary locations of climatological (i.e., time-mean) deep convection. We compare three fully-coupled GCMs that span a range of climatological regions of deep convection: CCSM4, in which the Labrador Sea is the primary deep convection region; GFDL ESM2M, in which the Irminger and Iceland Basins are the main deep convection regions; and HadGEM3-GC3.1-LL, in which the deep convection is concentrated in the GIN Seas. Our low-frequency component analysis provides a novel view of the mechanisms of low-frequency AMOC variability, its role in OHT, and its links to WMT variability.

This paper is organized as follows. In section 2a, we describe the models used in this analysis. In section 2b, we compare and contrast the model climatologies of Atlantic OHT and ocean circulation. In section 2c, we describe the models' climatologies of AMOC in density space. In section 2d, we examine the surface-forced overturning streamfunction and water-mass transformation in each model. In section 3, we compare the water-mass transformation computed from model data to the water-mass transformation calculated from observational datasets. In section 4, we use low-frequency component analysis and subsequent lead-lag regression analyses to elucidate the mechanisms of low-frequency OHT variability in the three models. In section 5, we summarize our results, describe our main conclusions, and compare what we have found to the results from other studies.

2. Model climatologies

a. Description of models

We examine the mechanisms of low-frequency Atlantic OHT variability within three coupled atmosphere-ocean GCM simulations: a 1300-year pre-industrial control simulation of CCSM4, a 500-year pre-industrial control simulation of GFDL ESM2M, and a 500-year pre-industrial control simulation of HadGEM3-GC3.1-LL, all of which have ocean-model resolution of $\sim 1^\circ$ in the midlatitudes. All three simulations are forced with constant 1850s greenhouse-gas and aerosol levels, with no volcanic eruptions. We chose these three GCMs for several reasons. First, AMOC and Atlantic OHT variability have been extensively documented within each GCM (Danabasoglu et al. 2012b,c; Dunne et al. 2012; MacMartin et al. 2013; Msadek et al. 2013; Zhang and Wang 2013; MacMartin et al. 2016; Kuhlbrodt et al. 2018; Menary et al. 2018; Docquier et al. 2019; Li et al. 2019; Jackson et al. 2020; Koenigk et al. 2020; Roberts et al. 2020). Second, they are comprised of three distinct and commonly-used ocean model components: CCSM4 uses the Parallel Ocean Program version 2 (POP2); GFDL-ESM2M uses the Modular Ocean Model version 4p1 (MOM4p1); and HadGEM3 uses the Nucleus for European Modelling of the Ocean version 3.6 (NEMO3.6). Finally, as noted above, the three models differ substantially in their locations of deep convection: CCSM4 shows deep convection primarily in the Labrador Sea; ESM2M shows deep convection primarily in the Irminger and Iceland Basins; and HadGEM3 shows deep convection primarily in the GIN Seas (Fig. 1a, b, c).

b. Atlantic OHT and ocean circulation

A comparison of the model climatologies of the ocean circulation and density structure along with the OHT gives context for the analysis of the variability. First, we consider the Atlantic OHT.

The climatological Atlantic OHT is similar in all three GCMs, with a peak at around 20°N (Fig. 2a, b, c), though the magnitude of the peak varies between them, with CCSM4 having the largest peak OHT and HadGEM3 having the smallest. The meridional structure of the OHT is calculated during run time for CCSM4 and HadGEM3. For GFDL-ESM2M, we use model output of total OHT calculated on the model's native grid, giving an accurate estimate of OHT through most of our study region since the grid is rectilinear south of 65°N.

Second, we look at the barotropic streamfunction and the depth-averaged ocean temperature. The depth-averaged potential temperature climatologies in the subpolar regions are also similar for the models, with cooler waters on the west side of the subpolar gyre and warmer waters to the east (Fig. 1d, e, f). However, while the large-scale features of the barotropic streamfunction patterns show the same salient features in all three GCMs, the subpolar gyre shapes and strengths vary substantially, although the maximum value for each model occurs near the mouth of the Labrador Sea. The subpolar gyre is strongest in CCSM4 (with a peak of 57.6 Sv), is weaker in ESM2M (peak of 37.1 Sv), and is weakest in HadGEM3 (peak of 30.8 Sv).

Finally, we analyze the winter mixed-layer depth climatologies, which indicate the regions where the deep convection is concentrated for each model. Mixed-layer depths are calculated during run time based on the vertical structure of density in the upper ocean (Levitus 1983; Large et al. 1994). The winter mixed-layer depth climatologies vary considerably between the three GCMs. In CCSM4, the winter mixed layers are deepest in the Labrador Sea, with some deep mixed layers in the Iceland and Irminger Basins as well (Fig. 1a). In GFDL ESM2M, mixed layers are much deeper than in CCSM4, and the deepest mixed layers are located in the Iceland and Irminger Basins, though there is a small band of deep mixed layers in the Labrador Sea (Fig. 1b). In HadGEM3, mixed layers are the shallowest of all the models, and the deepest mixed layers are located in the GIN Seas (Fig. 1c).

c. AMOC in density space

An examination of AMOC highlights the portion of the overturning circulation that is associated with deep sinking. Typically, the meridional overturning streamfunction calculated in depth space reaches its maximum in the midlatitudes, south of the subpolar region (Zhang 2010). In contrast, the meridional overturning streamfunction calculated in density space (AMOCσ) typically has a maximum farther north in the subpolar latitudes, as is also found in observational estimates (Talley et al. 2003). Thus, AMOCσ highlights the contribution from transport within the North Atlantic Deep Water (NADW) that flows southward along steep isopycnals nearly perpendicular to the isobars. This corresponds to a strong gradient in the meridional overturning streamfunction over an extremely narrow density range. In depth space, the AMOC maximum in NADW formation sites is hidden because northward transport in the east is compensated by southward transport in the west in the same depth layer (Zhang 2010). Thus, AMOCσ allows a focus on the evolution of water-mass properties as a function of latitude better than AMOC in depth space (Straneo 2006b; Pickart and Spall 2007).

For CCSM4, we calculate AMOCσ in density space (henceforth simply referred to simply as AMOC) using Eq. (1) from Newsom et al. 2016:

$$\mathrm{AMOC}(\sigma, y, t) = -\int_{x_W}^{x_E} \int_{-B(x,y)}^{z(x,y,\sigma,t)} v(x,y,z,t)\,dz\,dx, \tag{1}$$

where σ is the potential density referenced to 2000m, y is the latitude, x is longitude, x_W and x_E are the western and eastern longitudinal limits of the basin, respectively, v is the meridional velocity, z is depth (positive upwards), $B(x,y)$ is the bottom depth, and t is time. For GFDL ESM2M, we use model output of the AMOC. For HadGEM3, we use AMOC computed on the native grid (courtesy of Dr. Laura Jackson at the UK Meteorology Office).

The relative strength of AMOC and the density class where AMOC reaches its maximum for each model will become relevant when we later discuss the regressions of AMOC and the WMT onto the first LFC of OHT. The AMOC climatologies for CCSM4 and ESM2M are similar, though ESM2M's is weaker, and its maximum is shifted towards lower latitudes and slightly lighter densities (Fig. 2d, e). CCSM4's AMOC maximum of 29.1 Sv is located at 52.2° N and σ_2 = 36.69 kg/m^3. ESM2M's AMOC maximum of 27.4 Sv is located at 47.5° N and σ = 36.6 kg/m^3 (Fig. 2d, e). HadGEM3's AMOC maximum of 15.4 Sv, which is much weaker than that in CCSM4 or ESM2M, is located at 52.3° N and σ_2 = 36.5 kg/m^3 (Fig. 2f, i).

d. Surface-forced water-mass transformation and overturning streamfunction

The surface-forced WMT quantifies the density flux into the ocean due to surface buoyancy forcing (i.e., air-sea heat and freshwater fluxes). It also links changes in deep convection in different regions to changes in AMOC (Langehaug et al. 2012b). WMT is calculated from air-sea heat and freshwater fluxes (Tziperman 1986; Speer and Tziperman 1992; Langehaug et al. 2012b). Mixing also provides a substantial contribution to WMT (Nurser et al. 1999), often opposing the surface-forced WMT in the North Atlantic (Tandon and Zhao 2004), though it is generally much weaker than the surface-forced component outside of the tropics. Nurser et al. (1999) used a coupled model and estimated the magnitude of the total mixing component to be about 4 Sv in the subpolar North Atlantic, or about 40% as large as the surface-forced component. Here we neglect this contribution as the publicly available data do not have sufficient time resolution to examine the mixing component in these models.

Our WMT calculation follows the methods of Speer and Tziperman 1992. The surface density flux $D(x,y,t)$ is calculated via:

$$D(x,y,t) = \frac{\alpha(x,y,t)Q_H(x,y,t)}{c_w} - \beta(x,y,t)S(x,y,t)Q_F(x,y,t), \tag{2}$$

where the first and second terms are the heat and freshwater flux components respectively, both in units of kg m^{-2} s^{-1}; α is the thermal expansion coefficient; Q_H is the surface heat flux into the ocean in W m^{-2}; c_w is the specific heat capacity of seawater, assumed to be uniform and constant with a value of 4186 J kg^{-1} K^{-1}; β is the haline contraction coefficient; S is the surface absolute salinity; and Q_F is the freshwater flux in kg m^{-2} s^{-1}.

The surface-forced WMT at each density is calculated by integrating $D(x,y,t)$ over all surface area in each density bin:

$$F(\sigma) = \frac{1}{\Delta\sigma}\int_{\sigma}^{\sigma+\Delta\sigma} D(x,y,t)dA, \tag{3}$$

where $F(\sigma)$ is the surface forced WMT in Sv, $\sigma = \rho - 1000$ is the potential density referenced to 2000m in kg m^{-3}, and $\Delta\sigma$ is the width of each density bin.

We also examine the total $F(\sigma)$ in regions that encompass the Labrador Sea and the GIN Seas separately (for the location of these regions, see the marked boxes in Fig. 1). Here, the GIN Seas region is defined to also encompass the Iceland and Irminger Basins in order to include all deep convection in the models east of the Labrador Sea.

The partitioning of climatological WMT between the Labrador Sea and the GIN Seas differs substantially among the models (Fig. 3a, b, c). In CCSM4, because there are large areas with deep mixed layers not only in the Labrador Sea but also in the Iceland and Irminger Basins, both the Labrador Sea and GIN Seas regions contribute substantially to the WMT within the density range where AMOC is at or near its maximum (Fig. 3a). For both ESM2M and HadGEM3, the GIN Seas dominate the WMT at all density classes that outcrop in the models' deepwater formation regions (i.e., the regions with the deepest mixed layers). We compare the WMT computed from the models to what is found in observational datasets in section 3 below. In all three models, the thermal WMT component dominates over the haline component. The haline component provides a substantial opposing contribution in both the Labrador Sea and GIN Seas regions in the density range where AMOC is at its maximum (Fig. 3a, b, c). The haline component of WMT is most important in HadGEM3 and least important in GFDL ESM2M (Fig. 3b, c).

To understand how much of the structure of AMOC can be attributed to WMT, we compare the full AMOC from Eq. (1) against the surface-forced overturning streamfunction calculated following Marsh (2000) and Newsom et al. (2016). The surface-forced MOC is calculated from the divergence of the surface density flux:

$$F(\sigma, y, t) = -\frac{\partial}{\partial \sigma} \int \int_{A[\sigma^* > \sigma]} D(x, y, t) \mathcal{H}[\sigma - \sigma_{min}(y, t)] dA, \tag{4}$$

where $A[\sigma^* > \sigma]$ is the area of the region with surface density greater than σ; $D(x, y, t)$ is the density flux given by Eq. (2); $\mathcal{H}$ is the Heaviside function; $\sigma_{min}(y, t)$ is the lowest density to outcrop at latitude y and time t; and A is the surface area.

In both CCSM4 and ESM2M, there is a substantial discrepancy between the climatological surface-forced overturning streamfunction and the climatological full AMOC (Figs. 3d, e and 2d, e), which must be due to mixing. The maximum surface-forced MOC across all densities and all latitudes north of 35°N is equal to 34.8 Sv and 19.1 Sv for CCSM4 and ESM2M, respectively (Fig. 3d, e), whereas the maximum AMOC is equal to 29.9 Sv and 27.4 Sv respectively (Fig. 2d, e). In CCSM4, the mixing contribution to overturning is small, about 14% as large as the surface-forced term, and acts to weaken the overturning. In ESM2M, the mixing term is more substantial, about 43% as large as the surface-forced contribution, and acts to strengthen overturning. Substantial discrepancies between the surface-forced MOC and the total AMOC are not uncommon in models;

discrepancies as large as 15.4 Sv have been found in some models (Grist et al. 2009). The surface-forced AMOC is typically stronger than the total AMOC, but the reverse has been found in at least one model (Grist et al. 2009).

In HadGEM3, the surface-forced overturning streamfunction and full AMOC are similar in magnitude (Figs. 3f) and 2f). The maximum surface-forced MOC across all densities and all latitudes north of 35°N is equal to 14.6 Sv (Fig. 3f), and the maximum AMOC is equal to 15.4 Sv (Fig. 2f) such that there is a very small mixing contribution in this model, about 5% as large as the surface-forced component.

3. Comparison of model water mass transformation to observational datasets

To determine which of the GCMs has the most realistic representation of surface WMT, we compare WMT from each of the three models to WMT computed from oceanic and atmospheric observation-based datasets. We further consider whether model biases in sea-surface temperature, salinity, or air-sea surface fluxes are responsible for any discrepancies in WMT between the models and observations. To do so, we use monthly surface air-sea heat fluxes over the 26 year period 1984-2009 from the Objectively Analyzed Air-Sea Fluxes dataset (OAFlux; Yu and Weller 2008), monthly SSTs from NOAA Optimum Interpolation Sea Surface Temperature V2 (OISST; Reynolds et al. 2002) and surface salinities from the Hadley Centre's EN4.2.1 (Good and Rayner 2013). To estimate freshwater fluxes, we use monthly precipitation, evaporation, snow melt and river runoff data from the ECMWF atmospheric reanalysis (ERA5; Hersbach and Dee 2016). Precipitation and evaporation are taken directly from ERA-5 monthly averaged output, while river runoff is calculated by routing net precipitation over land (from ERA5) to the appropriate ocean grid point using the STN30p River Topology dataset (Vörösmarty et al. 2000), as described in Wills and Schneider (2015). We convolve the monthly observed surface fluxes with SSTs and surface salinities from the equivalent years (1984-2009) of OISST and EN4.2.1 to calculate the WMT and compare that to the WMT in models. We then swap out the observed sea-surface temperature and salinity for those fields taken from each of the models, comparing the resulting WMT with that derived from observations. Similarly, we repeat the calculation using observed sea-surface temperature and salinity fields but with the observed surface fluxes swapped for modeled fluxes.

Similar to the models, the observation-based WMT shows positive values in the Labrador Sea, Irminger and Iceland Basins, as well as the GIN Seas. There are also very large positive values along the Gulf Stream path. In all of these regions, strong, sustained winter heat loss to the atmosphere overwhelms any compensating effects from freshwater fluxes (Fig. 4a, d). The GIN Seas dominate the WMT at densities above approximately 35.8 kg/m^3. The freshwater components in both regions are negative, with a small but non-negligible magnitude corresponding to approximately 17% of that of the thermal component in the Labrador Sea and 22% in the GIN Seas. The WMT in the two regions occur over a larger range of densities compared to the WMT in models (Fig. 4g). Of the three models, HadGEM3 is the most similar to observations, though it still shows substantial discrepancies in the Gulf Stream Extension region.

To examine what features of the models control the differences with observations, we first convolve observation-based sea-surface temperatures and salinities with surface fluxes from the different models. Swapping out the observed surface heat and freshwater fluxes for CCSM4's results in a large increase in the magnitude of the thermal WMT component in the GIN Seas, and a smaller increase in the Labrador Sea (not shown). The magnitude of the freshwater component becomes substantially larger in both regions as well. Swapping out the observed surface heat and freshwater fluxes for ESM2M's yields a result that remains closer to the WMT computed from observations (not shown). Finally, swapping for HadGEM3's surface fluxes results in a WMT that is closest to observations, though there is still a substantial discrepancy in both components of the GIN Seas WMT (Fig. 4h).

Convolving the observed surface fluxes with CCMS4 SST and surface salinities causes the Labrador Sea WMT to be concentrated over a smaller density range and at a higher density class, and also yields substantially stronger thermal WMT in the GIN Seas (not shown). Swapping out the observed SSTs and salinities for ESM2M's causes both the Labrador Sea and GIN Seas WMT to be concentrated over smaller density ranges (not shown), with large, narrower peaks at $\sigma_2 = 36.6$ and $\sigma_2 = 36.7$ respectively. Swapping out the observed SSTs and salinities for HadGEM3's gives a result that is the most similar to what is found when using observational data (Fig. 4c, f, i). The freshwater WMT component becomes slightly smaller when using sea-surface temperatures and salinities from models, particularly when using GFDL-ESM2M and HadGEM3 SSTs and salinities.

Based on these results, it appears that biases in surface heat and freshwater fluxes are largely responsible for the discrepancy between WMT calculated from models and from observational data; biases in sea-surface temperatures and salinities play a secondary role. Although HadGEM3 is the most realistic of all the models in both its surface fluxes and surface temperatures and salinities, it still has substantial biases in freshwater fluxes relative to observations. This will be important to keep in mind when we consider the role of WMT variability in low-frequency OHT variability in these models in the following section.

4. Mechanisms of low-frequency OHT variability

To examine the controls on low-frequency OHT variability, we first apply a low-frequency component analysis (LFCA; Wills et al. 2018, 2019a) to Atlantic OHT in all three GCMs. We solve for the low-frequency patterns (LFPs) of the OHT, which are the linear combinations of the leading empirical orthogonal functions (EOFs) that maximize the ratio of low-frequency variance to total variance in their corresponding timeseries (called low-frequency components; LFCs). Low-frequency variance is defined as the variance that remains after the pointwise application of a Lanczos filter with a low-pass cutoff of 10 years. The 10-year low-pass filter is only used in identifying the LFPs, and all information about high-frequency variations in the data is preserved. LFCA is related to a broader class of statistical analyses that identify patterns that maximize the ratio of signal to noise (Allen and Smith 1997; Venzke et al. 1999; Schneider and Griffies 1999; Schneider and Held 2001; Ting et al. 2009). We focus on the first LFP/LFC (Fig. 5a, b, c, g, h, i), which has the highest ratio of low-frequency variance to total variance and is well separated in this ratio from the second LFP/LFC.

A traditional approach to studying AMOC variability is to composite on indices such as the AMOC index or a convective index (Delworth et al. 1993; Danabasoglu et al. 2012b; Langehaug et al. 2012b; Tulloch and Marshall 2012; MacMartin et al. 2013). Those indices explain a smaller fraction of low-frequency OHT variance than does the first LFC (Fig. 5 d, e, f), and also have a smaller signal-to-noise ratio. Another commonly-used metric, the first principal component of the low-pass filtered OHT, explains a similar amount of low-frequency variance (Fig. 5d, e, f), however, the loss of time resolution makes it difficult to discern lead-lag relationships (Cane et al. 2017; Wills et al. 2019a), precluding a full mechanistic understanding of the drivers of OHT changes. To determine the mechanisms driving low-frequency OHT variability, we compute lead-lag regressions between the LFC and anomalies in several atmospheric and ocean fields: upper ocean density, SLP, ocean heat content, WMT, AMOCσ, and the barotropic streamfunction, which characterizes the gyre circulation.

a. The pattern of low-frequency Atlantic OHT variability

The first LFP of Atlantic OHT represents the OHT anomaly associated with a one standard deviation (1σ) anomaly in the corresponding LFC time series. The first LFPs of CCSM4 and GFDL ESM2M are similar, i.e., they are both meridionally coherent with a narrow peak in the mid-latitudes around 45°N (Fig. 5a, b). The main difference is that GFDL ESM2M's LFP has a higher magnitude owing to stronger AMOC variability in that model (Yan et al. 2018). For HadGEM3, the magnitude of the first LFP of OHT is smaller than the other two models, with a broader peak in the mid-latitudes (Fig. 5c).

The regressions of the LFC and other indices onto the 10-year low-pass filtered OHT indicate that in all three models, the LFC indeed explains more low-frequency OHT variance than other indices, including the first PC of the non-low-pass filtered OHT, the AMOC index and the convective index (Fig. 5d, e, f). This indicates that although AMOC plays a major role in low-frequency OHT variability, there are other important processes that contribute to the variability as well. It is also evident that in CCSM4 and ESM2M, the LFP exhibits a similar pattern to the first PC of the low-pass filtered OHT, with the peaks almost exactly aligned, though it explains less low-frequency variance at some latitudes. In all models, the meridional structure of the LFC is more similar to the structure of the OHT regressed onto the AMOC index than the low-pass PC. The LFP creates an index that yields a similar time series to that of the low-pass PC but with all time resolution left intact; hence the LFP captures rapid transitions within low-frequency OHT variability (Fig. 5g, h, i). For HadGEM3, the LFC spatial pattern is different from what is found in the low-pass PC; the peak in the low-pass PC is located further south than that in the LFP, i.e., at 18.5°N vs. 45°N for the LFC (Fig. 5f), potentially because the low-pass PC aliases higher-frequency subtropical OHT variability.

b. Mechanisms of low-frequency OHT variability in CCSM4

In order to examine the mechanisms that drive low-frequency OHT variabilty, we next study lead-lag relationships between the first LFC time series and different oceanic and atmospheric variables. We begin the discussion of the results for CCSM4 before comparing to the other two models in the subsequent subsections. Lagged regressions between the LFC time series and the OHT reveals how the OHT pattern progresses leading up to and following the time of maximum OHT (Fig. 6a, d). These regressions indicate that at lead times (when OHT leads the LFC, i.e., prior to the time of maximum OHT), the OHT steadily increases in magnitude before reaching its maximum at lag zero with a peak at 45°N. (Fig. 6a). At lag times (i.e., after the time of maximum OHT), the OHT steadily decreases in magnitude. The OHT spatial pattern at lag times is different from the one at lead times, as there is a large change in gyre circulation after the time of maximum OHT, causing an abrupt jump in OHT at the boundary between the subtropical and subpolar gyres (cf. Fig. 10f).

Lagged regressions between the LFC and SLP, as well as the associated wind stress anomalies, reveal the role that atmospheric forcing plays in driving the OHT variability. In the eight years before the time of maximum OHT (Fig. 7a-c shows leads up to 6 years), there is a persistent SLP pattern associated with anomalous northwesterly winds off eastern North America. This pattern is similar to the NAO, but the center of the high-pressure system is northwest of where it appears in the NAO SLP pattern in observations. Since the persistence time scale of SLP anomalies is less than one month (Ambaum and Hoskins 2002), the persistence of this pattern must be due to memory in the ocean. At lead 2 years, this pattern becomes more zonal before intensifying during the time of maximum OHT. This intensification corresponds to Ekman transport that reinforces the low-frequency OHT pattern, which shows up because high-frequency variability is not completely filtered out by the LFCA. This intensification does not occur when the data are low-pass filtered (not shown). Only weak SLP anomalies remain after the maximum OHT (Fig. 7f), indicating a weak atmospheric response to this variability.

The anomalous winds at lead times drive cooling and densification of near-surface Labrador Sea waters (Fig. 8a-c), resulting in enhanced convection. This increase in convection strengthens the AMOC at lead times. The AMOC then carries anomalously warm water northward into the subpolar gyre starting at lead 2 years. The gyre circulation then carries this water into the Labrador Sea, where it eliminates the positive density anomalies and hence the anomalous convection (Fig. 8d-f). Meanwhile, a persistent positive density anomaly forms in the Gulf Stream Extension region, suggesting a southward shift of the North Atlantic Current and Gulf Stream.

Owing to the increase in Labrador Sea convection, AMOC strengthens at lead times in the high latitudes, beginning around nine years before the maximum OHT. This AMOC anomaly extends throughout the North Atlantic, and is centered around 56° N and σ_2 = 36.82, where it reaches a maximum of 2.1 Sv (Fig. 9e). This is farther north and at a higher density class than the maximum climatological AMOC. Leading up to the time of maximum OHT, this anomaly intensifies and spreads southwards and to lower densities. AMOC reaches its maximum strength when the OHT is at its maximum (i.e., at lag 0). At lag times, AMOC steadily declines as a result of the weakened convection in the Labrador Sea (Fig. 9d-f).

Leading up to the time of the maximum OHT, both the subpolar and subtropical gyres strengthen and the subpolar gyre cools (Fig. 10a-e). At lag times, the barotropic anomalies become concentrated around the boundary between the subpolar and subtropical gyres, and there is a persistent cold anomaly in the Gulf Stream Extension region (Fig. 10f).

As the Labrador Sea water densifies at lead times, WMT increases there (Fig. 11a), peaking two years before maximum OHT and AMOC. This increase in WMT is centered around σ_2 = 36.87, where it reaches a maximum of 2.9 Sv. This is at a higher density class than the maximum AMOC anomaly, though it still coincides with the large, broad AMOC anomaly. There is only a small change in WMT in the GIN Seas (Fig. 11d), indicating that the Labrador Sea WMT changes are the primary driver of low-frequency OHT and AMOC variability in CCSM4. The WMT changes are overwhelmingly dominated by heat-flux changes (Fig. 12a, d).

c. Comparison to mechanisms of low-frequency OHT variability in GFDL-ESM2M

Applying the same analysis to ESM2M, we find that OHT also strengthens leading up to the time of maximum OHT (Fig. 6b). At lag times, OHT steadily decreases, as expected, eventually becoming negative at lag 6, indicating periodicity in this model's OHT variability (Fig. 6e). This has been reported in previous studies (Dunne et al. 2012) and is evident as a peak in the OHT and AMOC power spectra at 15 years (not shown). This periodicity is not found in either of the other two GCMs examined here.

The SLP pattern at lead times is similar to what is found in CCSM4, with a high pressure system over the Labrador region of Canada driving anomalous northwesterly winds over the Labrador Sea (Fig. 7g), though the intense high pressure system found in CCSM4 at lag 0 is not found in ESM2M. Similar to CCSM4, SLP anomalies are weak at lag times (Fig. 7i), though ESM2M does show negative SLP anomalies throughout the North Atlantic.

The anomalous northwesterly winds over the Labrador Sea drive near-surface cooling and densification in the region at lead times (Fig. 8g), albeit less pronounced than in CCSM4. This strengthens convection in the Labrador Sea, which then causes AMOC to strengthen. Similar to CCSM4, the intensified AMOC then reduces the density anomalies and high latitude convection (Fig. 8h-i). Meanwhile, density anomalies propagate southward along the western boundary, a process not seen in either of the other models.

Similar to CCSM4, AMOC begins to strengthen about six years prior to the maximum OHT. However, unlike in CCSM4, as the AMOC anomaly intensifies, it begins to propagate southward, similar what is found for the density anomalies (Fig. 9h). At lag times, the AMOC anomaly rapidly dissipates and continues to propagate southward, after which it is replaced by a smaller negative AMOC anomaly at high latitudes (Fig. 9i), which we do not find in CCSM4. The AMOC anomaly at the time of maximum OHT is centered around σ_2 = 36.69 and θ = 44.5°N, with a maximum value of 2 Sv. This is south of and at a higher density class than the maximum climatological AMOC in this model.

Similar to CCSM4, while AMOC strengthens at lead times, both the subpolar and subtropical gyres strengthen and the subpolar gyre cools (Fig. 10g). Starting about one year before the maximum OHT, the barotropic streamfunction anomalies begin to congregate around the gyre boundary (not shown). This anomaly continues to propagate along the western boundary. Even though climatological deep convection in GFDL-ESM2M is focused in the Irminger and Iceland Basins, the lagged regressions of WMT onto the first LFC look surprisingly similar to CCSM4, with a much more pronounced peak in the Labrador Sea at lead times than in the GIN Seas box (which also includes the Irminger and Iceland Basins). The WMT anomaly in the Labrador Sea at lead 2 years is centered at σ_2 = 36.76 with a maximum value of 1.6 Sv. The WMT in the GIN Seas starts out with a positive anomaly at lead 4 years, centered around σ_2 = 36.68 with a maximum value of 0.3 Sv, before it becomes negative at lead 2 years (Fig. 11b, e). Both the Labrador Sea and GIN Seas WMT variability show substantial periodicity, as found with the other variables in this model. The WMT variability is dominated by heat flux changes, with freshwater flux changes playing a minor role (Fig. 12b, e).

d. Comparison to mechanisms of low-frequency OHT variability in HadGEM3

For HadGEM3, OHT gradually strengthens leading up to the time of maximum OHT, maintaining a similar pattern with a very broad peak in the mid-latitudes (Fig. 6c). At lag times, the OHT gradually weakens. This process is much more gradual than it is in the other models (Fig. 6f).

The SLP pattern is slightly more zonal than it is in the other models at most lead times (not shown), with a pronounced high-pressure system over Labrador only occurring between lead 5 and lead 3 (Fig. 7j). At lead 1, this NAO-like pattern disappears and at lag zero there is a high pressure system over the eastern subpolar gyre and the Iceland Basin, similar to what is found in CCSM4, albeit much weaker. Immediately after lag zero, the SLP anomalies become small (Fig. 7l), similar to what is found in the other two models.

As seen in the other two GCMs, there is pronounced densification in both the Labrador Sea and the Irminger and Iceland Basins at lead times (Fig. 8j), peaking at lead 2 years. This drives increased convection in these regions, strengthening AMOC, which then acts to weaken the high-latitude convection by carrying anomalously warm water northward (Fig. 8l). This warm water enters the subpolar gyre via the Iceland and Irminger Basins, and does not have as much of a pronounced density anomaly as seen in CCSM4. Similar to CCSM4, there is a persistent positive density anomaly in the Gulf Stream Extension region, and in contrast to ESM2M there is no southward propagation of upper ocean density anomalies.

As in CCSM4, AMOC strengthens at lead times, reaching a maximum at lag zero, coinciding with the time of maximum OHT (Fig. 9j-k). Afterwards, it steadily weakens as a result of the reduced convection (Fig. 9l). The AMOC anomaly at the time of maximum OHT is centered around $\sigma_2 = 36.63$ and $\theta = 55.6°$N, with a maximum value of 1.3 Sv. This is north of and at a higher density class than the maximum climatological AMOC in this model.

At lead times, while AMOC strengthens, the subpolar gyre also strengthens, and at lag times, the positive anomalies become more concentrated at the boundary between the subpolar and subtropical gyres (Fig. 10j-l), as seen in the other models.

Although the climatological deep convection in HadGEM3 primarily occurs in the GIN Seas (Fig. 3e), the WMT regressions at lead times show that most of the WMT variability occurs in the Labrador Sea. There is a pronounced increase in WMT in the Labrador Sea at lead times, with a peak at lead 2 years, as in the other models. The anomaly at lead 2 years is centered at $\sigma_2 = 36.74$ with a maximum value of 0.9 Sv (Fig. 11c). There is also a peak in the GIN Seas at lead 2, but it is not as pronounced, with a maximum magnitude equal to half of what is found in the Labrador Sea, i.e., 0.44 Sv (Fig. 11f). The WMT variability in this model is dominated by heat flux changes, though freshwater fluxes do contribute more than in the other models (Fig. 12c, f), providing a small negative contribution to the WMT at lead times.

5. Discussion and Conclusions

Our results suggest a mechanism for low-frequency North Atlantic OHT variability that is consistent across the three distinct GCMs used here: persistent SLP anomalies in the 4-9 years prior to the time of maximum OHT, which are associated with anomalous northwesterly winds off eastern North America that cool and densify the Labrador Sea waters through air-sea heat fluxes, increasing convection in that region. This increased convection causes AMOC to strengthen, increasing the OHT as a result. The strengthened AMOC carries anomalous warm water northward into the subpolar gyre, which then carries it into the Labrador Sea, where it shuts down the anomalous convection and weakens AMOC and OHT.

Although this mechanism is similar across the models, in GFDL-ESM2M there is pronounced periodicity in the density, AMOC, OHT and water-mass transformation variability. AMOC anomalies also appear to propagate southward in that model, consistent with what was found in Zhang (2010).

Our results also suggest that AMOC variability is closely linked to preceding density anomalies in the subpolar gyre and the Labrador Sea, consistent with mechanisms discussed in Tulloch and Marshall (2012) and Kwon and Frankignoul (2014). However, these findings are not in agreement with those of Dong and Sutton (2005), who found a salinity dominated mechanism in HadCM3, where a strengthened North Atlantic Current causes an increase in deep convection in the GIN Seas.

Based on the comparison with observations, it is clear that biases in surface heat and freshwater fluxes play a much larger role than sea-surface temperatures and salinities in setting the discrepancies between model and observation-based WMT. Also, it appears that HadGEM3 has the most realistic surface heat fluxes, sea-surface temperatures and salinities of the three models used here, though HadGEM3 heat fluxes in both the Labrador Sea and GIN Seas are still larger than OAFlux estimates, and there are still substantial temperature and salinity biases in both regions in this model. HadGEM3's freshwater fluxes are not any more realistic than what is found in the other models.

The lead-lag regression analysis of water mass transformation suggests that regardless of the model's primary location of climatological convection, the Labrador Sea appears to play a dominant role in driving low-frequency AMOC and OHT variability. In CCSM4, climatological convection is concentrated in the Labrador Sea, and the GIN Seas play only a minor role in driving the AMOC and OHT variability. In GFDL-ESM2M, climatological convection is primarily in the Irminger and Iceland Basins, but the Labrador Sea plays a more dominant role in driving the AMOC variability, with the GIN Seas and the Irminger and Iceland Basins playing a significant but more minor role. In HadGEM3, the climatological convection is mainly in the GIN Seas, yet the Labrador Sea still contributes twice as much as the GIN Seas to the WMT anomalies associated with AMOC and OHT variability. Though not necessarily all of the anomalous surface-forced WMT in the Labrador Sea translates to anomalous overturning owing to compensation from mixing processes, the robust lead-lag relationship we have found suggests a mechanistic link between the low-frequency OHT variability and the WMT in the Labrador Sea. The Labrador Sea also dominates the changes when applying the low-frequency component analysis to AMOC in each model instead of the OHT (not shown), indicating a clear link between WMT in the Labrador Sea and low-frequency AMOC variability as well.

In CCSM4 and ESM2M, which both have warm, salty biases in the Labrador Sea relative to observations, heat fluxes dominate the WMT variability, consistent with what was found by Menary et al. (2015b). This also holds true in HadGEM3, even though it does not have the same biases in the Labrador Sea. Freshwater fluxes play a more substantial role in the WMT climatology in HadGEM3, although the heat fluxes still dominate the variability.

Recent observations from the Overturning in the Subpolar North Atlantic Program (OSNAP) suggest that the Labrador Sea plays a minor role in driving the climatological overturning in the North Atlantic compared to the GIN Seas (Lozier et al. 2019; Zou et al. 2020). Zou et al. (2020) found that density compensation in the Labrador Sea is responsible for this, i.e., warm, salty water that enters the Labrador Sea exits as cold, fresh water in the same density class. They also show that large salinity biases in the Labrador Sea are responsible for the discrepancy between models and observations, as these biases may lead to a temperature dominated density structure, which is in agreement with what we have found here. The OSNAP data set is only 21 months long, and hence it was not possible to discern the mechanisms controlling decadal and multidecadal variability. In addition, Menary et al. (in review) and Lozier and Jackson (2020) both show that HadGEM3 is consistent with observational datasets and OSNAP data. Yet, the Labrador Sea dominates the low-frequency AMOC and OHT variability in HadGEM3. This suggests that the Labrador Sea may still dominate the low-frequency WMT, AMOC, and OHT variability in nature despite its limited role in setting the WMT and AMOC climatologies.

There are several caveats to our analysis. Both CCSM4 and ESM2M have substantial temperature and salinity biases in the Labrador Sea (Menary et al. 2015b), which could distort the representation of deep convection and overturning in these models. The low-resolution models used here also likely overestimate Labrador Sea convection because they do not resolve eddies, which play a significant role in Labrador Sea stratification (Straneo 2006a; Brandt et al. 2007; Garcia-Quintana et al. 2019). Another issue is that Nordic Seas overflow processes, which play an important role in AMOC and occur at relatively small spatial scales (Treguier et al. 2005; Langehaug et al. 2012a), are too weak in many low-resolution ocean models (Bailey et al. 2005). However, CCSM4 includes parameterized overflows, yet still shows similar behavior to what is found in the other two models (Danabasoglu et al. 2012a). Based on this, it would be valuable to perform a similar analysis in a high-resolution coupled model.

Here we have found that the Labrador Sea dominates low-frequency variability in water-mass transformation, meridional overturning, and Atlantic OHT in three models with distinct primary climatological deep water formation regions. The consensus between the three distinct models studied here, including a model which reproduces observations in the Eastern North Atlantic from the OSNAP program, suggests that the mechanisms that control decadal variability of the subpolar North Atlantic in these models may be representative of what is found in nature.

Data availability statement. The CMIP5 data for this study are accessible at the Earth System Grid Federation (ESGF) Portal (https://esgf-node.llnl.gov/search/cmip5/). The CMIP6 data for this study are accessible at the ESGF Portal (https://esgf-node.llnl.gov/search/cmip6/).

EN4.2.1 sea surface temperature and salinity data (downloaded on 2 March 2020) are available at https://www.metoffice.gov.uk/hadobs/en4/index.html. OISST monthly sea surface temperature data are available at https://psl.noaa.gov/data/gridded/data.noaa.oisst.v2.html. OAFlux data are available at http://oaflux.whoi.edu/index.html. ERA5 data are available at https://climate.copernicus.eu/climate-reanalysis.

Acknowledgments. The authors are grateful for support from the National Science Foundation through grants OCE-1523641 and OCE-1850900 (D. O. and K. C. A.); and AGS-1929775 (R. C. J. W.). We thank the CMIP5 and CMIP6 climate modeling groups for making their model output available. MATLAB and Python code for LFCA is available at https://github.com/rcjwills/lfca.

References

Allen, M. R., and L. A. Smith, 1997: Optimal filtering in singular spectrum analysis. *Physics Letters A*, **234 (6)**, 419 – 428, doi:https://doi.org/10.1016/S0375-9601(97)00559-8, URL http://www.sciencedirect.com/science/article/pii/S0375960197005598.

Ambaum, M. H. P., and B. J. Hoskins, 2002: The nao troposphere–stratosphere connection. *Journal of Climate*, **15 (14)**, 1969–1978, doi:10.1175/1520-0442(2002)015<1969:TNTSC>2.0.CO;2, URL https://doi.org/10.1175/1520-0442(2002)015<1969:TNTSC>2.0.CO;2, https://doi.org/10.1175/1520-0442(2002)015<1969:TNTSC>2.0.CO;2.

Bailey, D. A., P. B. Rhines, and S. Häkkinen, 2005: Formation and pathways of north atlantic deep water in a coupled ice–ocean model of the arctic–north atlantic oceans. *Climate Dynamics*, **25 (5)**, 497–516, doi:10.1007/s00382-005-0050-3, URL https://doi.org/10.1007/s00382-005-0050-3.

Bjerknes, J., 1964: Atlantic air-sea interaction. Advances in Geophysics, Vol. 10, Elsevier, 1 – 82, doi:https://doi.org/10.1016/S0065-2687(08)60005-9, URL http://www.sciencedirect.com/

science/article/pii/S0065268708600059.

Brambilla, E., and L. D. Talley, 2008: Subpolar mode water in the northeastern atlantic: 1. averaged properties and mean circulation. *Journal of Geophysical Research: Oceans*, **113 (C4)**, doi:10.1029/2006JC004062, URL https://agupubs.onlinelibrary.wiley.com/doi/abs/10.1029/2006JC004062, https://agupubs.onlinelibrary.wiley.com/doi/pdf/10.1029/2006JC004062.

Brandt, P., A. Funk, L. Czeschel, C. Eden, and C. W. Böning, 2007: Ventilation and transformation of labrador sea water and its rapid export in the deep labrador current. *Journal of Physical Oceanography*, **37 (4)**, 946–961, doi:10.1175/JPO3044.1, URL https://doi.org/10.1175/JPO3044.1, https://doi.org/10.1175/JPO3044.1.

Brodeau, L., and T. Koenigk, 2016: Extinction of the northern oceanic deep convection in an ensemble of climate model simulations of the 20th and 21st centuries. *Climate Dynamics*, **46 (9)**, 2863–2882, doi:10.1007/s00382-015-2736-5, URL https://doi.org/10.1007/s00382-015-2736-5.

Cane, M. A., A. C. Clement, L. N. Murphy, and K. Bellomo, 2017: Low-pass filtering, heat flux, and atlantic multidecadal variability. *Journal of Climate*, **30 (18)**, 7529–7553, doi:10.1175/JCLI-D-16-0810.1, URL https://doi.org/10.1175/JCLI-D-16-0810.1, https://doi.org/10.1175/JCLI-D-16-0810.1.

Chafik, L., and T. Rossby, 2019: Volume, heat, and freshwater divergences in the subpolar north atlantic suggest the nordic seas as key to the state of the meridional overturning circulation. *Geophysical Research Letters*, **46 (9)**, 4799–4808, doi:10.1029/2019GL082110, URL https://agupubs.onlinelibrary.wiley.com/doi/abs/10.1029/2019GL082110, https://agupubs.onlinelibrary.wiley.com/doi/pdf/10.1029/2019GL082110.

Chylek, P., N. Hengartner, G. Lesins, J. D. Klett, O. Humlum, M. Wyatt, and M. K. Dubey, 2014: Isolating the anthropogenic component of arctic warming. *Geophysical Research Letters*, **41 (10)**, 3569–3576, doi:10.1002/2014GL060184, URL http://dx.doi.org/10.1002/2014GL060184, 2014GL060184.

Covey, C., and S. L. Thompson, 1989: Testing the effects of ocean heat transport on climate. *Global and Planetary Change*, **1 (4)**, 331 – 341, doi:https://doi.org/10.1016/0921-8181(89)90009-X, URL http://www.sciencedirect.com/science/article/pii/092181818990009X.

Danabasoglu, G., S. C. Bates, B. P. Briegleb, S. R. Jayne, M. Jochum, W. G. Large, S. Peacock, and S. G. Yeager, 2012a: The CCSM4 Ocean Component. *Journal of Climate*, **25 (5)**, 1361–1389, doi:10.1175/JCLI-D-11-00091.1, URL https://doi.org/10.1175/JCLI-D-11-00091.1, https://journals.ametsoc.org/jcli/article-pdf/25/5/1361/3992339/jcli-d-11-00091_1.pdf.

Danabasoglu, G., S. G. Yeager, Y.-O. Kwon, J. J. Tribbia, A. S. Phillips, and J. W. Hurrell, 2012b: Variability of the atlantic meridional overturning circulation in ccsm4. *Journal of Climate*, **25 (15)**, 5153–5172, doi:10.1175/JCLI-D-11-00463.1, URL https://doi.org/10.1175/JCLI-D-11-00463.1, https://doi.org/10.1175/JCLI-D-11-00463.1.

Danabasoglu, G., S. G. Yeager, Y.-O. Kwon, J. J. Tribbia, A. S. Phillips, and J. W. Hurrell, 2012c: Variability of the atlantic meridional overturning circulation in ccsm4. *Journal of Climate*, **25 (15)**, 5153–5172, doi:10.1175/JCLI-D-11-00463.1, URL https://doi.org/10.1175/JCLI-D-11-00463.1, https://doi.org/10.1175/JCLI-D-11-00463.1.

Day, J. J., J. C. Hargreaves, J. D. Annan, and A. Abe-Ouchi, 2012: Sources of multi-decadal variability in arctic sea ice extent. *Environmental Research Letters*, **7 (3)**, 034 011, URL http://stacks.iop.org/1748-9326/7/i=3/a=034011.

Delworth, T., S. Manabe, and R. J. Stouffer, 1993: Interdecadal variations of the thermohaline circulation in a coupled ocean-atmosphere model. *Journal of Climate*, **6 (11)**, 1993–2011, doi:10.1175/1520-0442(1993)006<1993:IVOTTC>2.0.CO;2, URL https://doi.org/10.1175/1520-0442(1993)006<1993:IVOTTC>2.0.CO;2, https://doi.org/10.1175/1520-0442(1993)006<1993:IVOTTC>2.0.CO;2.

Delworth, T. L., and F. Zeng, 2016: The impact of the north atlantic oscillation on climate through its influence on the atlantic meridional overturning circulation. *Journal of Climate*, **29 (3)**, 941–962, doi:10.1175/JCLI-D-15-0396.1, URL https://doi.org/10.1175/JCLI-D-15-0396.1, https://doi.org/10.1175/JCLI-D-15-0396.1.

Delworth, T. L., F. Zeng, G. A. Vecchi, X. Yang, L. Zhang, and R. Zhang, 2016: The north atlantic oscillation as a driver of rapid climate change in the northern hemisphere. *Nature Geosci*, **9 (7)**, 509–512, URL http://dx.doi.org/10.1038/ngeo2738.

Delworth, T. L., R. Zhang, and M. E. Mann, 2007: *Decadal to Centennial Variability of the Atlantic from Observations and Models*, 131–148. American Geophysical Union (AGU), doi:10.1029/173GM10, URL https://agupubs.onlinelibrary.wiley.com/doi/abs/10.1029/173GM10, https://agupubs.onlinelibrary.wiley.com/doi/pdf/10.1029/173GM10.

Deser, C., M. A. Alexander, S.-P. Xie, and A. S. Phillips, 2010: Sea surface temperature variability: Patterns and mechanisms. *Annual Review of Marine Science*, **2 (1)**, 115–143, doi:10.1146/annurev-marine-120408-151453, URL https://doi.org/10.1146/annurev-marine-120408-151453, pMID: 21141660, https://doi.org/10.1146/annurev-marine-120408-151453.

Docquier, D., and Coauthors, 2019: Impact of model resolution on arctic sea ice and north atlantic ocean heat transport. *Climate Dynamics*, **53 (7)**, 4989–5017, doi:10.1007/s00382-019-04840-y, URL https://doi.org/10.1007/s00382-019-04840-y.

Dong, B., and R. Sutton, 2002: Variability in north atlantic heat content and heat transport in a coupled ocean–atmosphere gcm. *Climate Dynamics*, **19 (5)**, 485–497, doi:10.1007/s00382-002-0239-7, URL https://doi.org/10.1007/s00382-002-0239-7.

Dong, B., and R. T. Sutton, 2003: Variability of atlantic ocean heat transport and its effects on the atmosphere. *Annals of Geophysics*, **46 (1)**, doi:10.4401/ag-3391, URL https://www.annalsofgeophysics.eu/index.php/annals/article/view/3391.

Dong, B., and R. T. Sutton, 2005: Mechanism of interdecadal thermohaline circulation variability in a coupled ocean–atmosphere gcm. *Journal of Climate*, **18 (8)**, 1117–1135, doi:10.1175/JCLI3328.1, URL https://doi.org/10.1175/JCLI3328.1, https://doi.org/10.1175/JCLI3328.1.

Dong, B.-W., and R. T. Sutton, 2001: The dominant mechanisms of variability in atlantic ocean heat transport in a coupled ocean-atmosphere gcm. *Geophysical Research Letters*, **28 (12)**, 2445–2448, doi:10.1029/2000GL012531, URL https://agupubs.onlinelibrary.wiley.com/doi/abs/10.1029/2000GL012531, https://agupubs.onlinelibrary.wiley.com/doi/pdf/10.1029/2000GL012531.

Drijfhout, S. S., and W. Hazeleger, 2006: Changes in moc and gyre-induced atlantic ocean heat transport. *Geophysical Research Letters*, **33 (7)**, doi:10.1029/2006GL025807, URL https://agupubs.onlinelibrary.wiley.com/doi/abs/10.1029/2006GL025807, https://agupubs.onlinelibrary.wiley.com/doi/pdf/10.1029/2006GL025807.

Dunne, J. P., and Coauthors, 2012: Gfdl's esm2 global coupled climate–carbon earth system models. part i: Physical formulation and baseline simulation characteristics. *Journal of Climate*, **25 (19)**, 6646–6665, doi:10.1175/JCLI-D-11-00560.1, URL https://doi.org/10.1175/JCLI-D-11-00560.1, https://doi.org/10.1175/JCLI-D-11-00560.1.

Dunne, J. P., and Coauthors, 2013: Gfdl's esm2 global coupled climate–carbon earth system models. part ii: Carbon system formulation and baseline simulation characteristics. *Journal of Climate*, **26 (7)**, 2247–2267, doi:10.1175/JCLI-D-12-00150.1, URL https://doi.org/10.1175/JCLI-D-12-00150.1, https://doi.org/10.1175/JCLI-D-12-00150.1.

Eden, C., and T. Jung, 2001: North atlantic interdecadal variability: Oceanic response to the north atlantic oscillation (1865–1997). *Journal of Climate*, **14 (5)**, 676–691, doi:10.1175/1520-0442(2001)014<0676:NAIVOR>2.0.CO;2, URL https://doi.org/10.1175/1520-0442(2001)014<0676:NAIVOR>2.0.CO;2, https://doi.org/10.1175/1520-0442(2001)014<0676:NAIVOR>2.0.CO;2.

Ganachaud, A., and C. Wunsch, 2000: Improved estimates of global ocean circulation, heat transport and mixing from hydrographic data. *Nature*, **408 (6811)**, 453–457, doi:10.1038/35044048, URL https://doi.org/10.1038/35044048.

Ganachaud, A., and C. Wunsch, 2003: Large-scale ocean heat and freshwater transports during the world ocean circulation experiment. *Journal of Climate*, **16 (4)**, 696–705, doi:10.1175/1520-0442(2003)016<0696:LSOHAF>2.0.CO;2, URL https://doi.org/10.1175/1520-0442(2003)016<0696:LSOHAF>2.0.CO;2, https://doi.org/10.1175/1520-0442(2003)016<0696:LSOHAF>2.0.CO;2.

Garcia-Quintana, Y., P. Courtois, X. Hu, C. Pennelly, D. Kieke, and P. G. Myers, 2019: Sensitivity of labrador sea water formation to changes in model resolution, atmospheric forcing, and freshwater input. *Journal of Geophysical Research: Oceans*, **124 (3)**, 2126–2152, doi:10.1029/2018JC014459, URL https://agupubs.onlinelibrary.wiley.com/doi/abs/10.1029/2018JC014459, https://agupubs.onlinelibrary.wiley.com/doi/pdf/10.1029/2018JC014459.

Gent, P. R., and Coauthors, 2011: The community climate system model version 4. *Journal of Climate*, **24 (19)**, 4973–4991, doi:10.1175/2011JCLI4083.1, URL https://doi.org/10.1175/2011JCLI4083.1, https://doi.org/10.1175/2011JCLI4083.1.

Good, M. J. M., S. A., and N. A. Rayner, 2013: En4: quality controlled ocean temperature and salinity profiles and monthly objective analyses with uncertainty estimates. *Journal of Geophysical Research: Oceans*, **118**, 6704–6716.

Grist, J. P., R. Marsh, and S. A. Josey, 2009: On the relationship between the north atlantic meridional overturning circulation and the surface-forced overturning streamfunction. *Journal of Climate*, **22 (19)**, 4989–5002, doi:10.1175/2009JCLI2574.1, URL https://doi.org/10.1175/2009JCLI2574.1, https://doi.org/10.1175/2009JCLI2574.1.

Hersbach, H., and D. Dee, 2016: Era5 reanalysis is in production. *ECMWF newsletter*, **147 (7)**, 5–6.

Isachsen, P. E., C. Mauritzen, and H. Svendsen, 2007: Dense water formation in the nordic seas diagnosed from sea surface buoyancy fluxes. *Deep Sea Research Part I: Oceanographic Research Papers*, **54 (1)**, 22 – 41, doi:https://doi.org/10.1016/j.dsr.2006.09.008, URL http://www.sciencedirect.com/science/article/pii/S0967063706002573.

Jackson, L. C., and Coauthors, 2020: Impact of ocean resolution and mean state on the rate of amoc weakening. *Climate Dynamics*, doi:10.1007/s00382-020-05345-9, URL https://doi.org/10.1007/s00382-020-05345-9.

Josey, S. A., J. P. Grist, and R. Marsh, 2009: Estimates of meridional overturning circulation variability in the north atlantic from surface density flux fields. *Journal of Geophysical Research: Oceans*, **114 (C9)**, doi:10.1029/2008JC005230, URL https://agupubs.onlinelibrary.wiley.com/doi/abs/10.1029/2008JC005230, https://agupubs.onlinelibrary.wiley.com/doi/pdf/10.1029/2008JC005230.

Kim, W. M., S. Yeager, P. Chang, and G. Danabasoglu, 2018: Low-frequency north atlantic climate variability in the community earth system model large ensemble. *Journal of Climate*, **31 (2)**, 787–813, doi:10.1175/JCLI-D-17-0193.1, URL https://doi.org/10.1175/JCLI-D-17-0193.1, https://doi.org/10.1175/JCLI-D-17-0193.1.

Kim, W. M., S. Yeager, and G. Danabasoglu, 2020: Atlantic multidecadal variability and associated climate impacts initiated by ocean thermohaline dynamics. *Journal of Climate*, **33 (4)**, 1317–1334, doi:10.1175/JCLI-D-19-0530.1, URL https://doi.org/10.1175/JCLI-D-19-0530.1, https://doi.org/10.1175/JCLI-D-19-0530.1.

Knight, J. R., R. J. Allan, C. K. Folland, M. Vellinga, and M. E. Mann, 2005: A signature of persistent natural thermohaline circulation cycles in observed climate. *Geophysical Research Letters*, **32 (20)**, doi:10.1029/2005GL024233, URL https://agupubs.onlinelibrary.wiley.com/doi/abs/10.1029/2005GL024233, https://agupubs.onlinelibrary.wiley.com/doi/pdf/10.1029/2005GL024233.

Koenigk, T., and Coauthors, 2020: Deep water formation in the north atlantic ocean in high resolution global coupled climate models. *Ocean Science Discussions*, **2020**, 1–39, doi:10.5194/os-2020-41, URL https://os.copernicus.org/preprints/os-2020-41/.

Kuhlbrodt, T., and Coauthors, 2018: The low-resolution version of hadgem3 gc3.1: Development and evaluation for global climate. *Journal of Advances in Modeling Earth Sys-*

tems, **10 (11)**, 2865–2888, doi:10.1029/2018MS001370, URL https://agupubs.onlinelibrary.wiley.com/doi/abs/10.1029/2018MS001370, https://agupubs.onlinelibrary.wiley.com/doi/pdf/10.1029/2018MS001370.

Kushnir, Y., 1994: Interdecadal variations in north atlantic sea surface temperature and associated atmospheric conditions. *Journal of Climate*, **7 (1)**, 141–157, doi:10.1175/1520-0442(1994)007<0141:IVINAS>2.0.CO;2, URL https://doi.org/10.1175/1520-0442(1994)007<0141:IVINAS>2.0.CO;2, https://doi.org/10.1175/1520-0442(1994)007<0141:IVINAS>2.0.CO;2.

Kwon, Y.-O., and C. Frankignoul, 2014: Mechanisms of multidecadal atlantic meridional overturning circulation variability diagnosed in depth versus density space. *Journal of Climate*, **27 (24)**, 9359–9376, doi:10.1175/JCLI-D-14-00228.1, URL https://doi.org/10.1175/JCLI-D-14-00228.1, https://doi.org/10.1175/JCLI-D-14-00228.1.

Langehaug, H. R., I. Medhaug, T. Eldevik, and O. H. Otterå, 2012a: Arctic/atlantic exchanges via the subpolar gyre. *Journal of Climate*, **25 (7)**, 2421–2439, doi:10.1175/JCLI-D-11-00085.1, URL https://doi.org/10.1175/JCLI-D-11-00085.1, https://doi.org/10.1175/JCLI-D-11-00085.1.

Langehaug, H. R., P. B. Rhines, T. Eldevik, J. Mignot, and K. Lohmann, 2012b: Water mass transformation and the north atlantic current in three multicentury climate model simulations. *Journal of Geophysical Research: Oceans*, **117 (C11)**, doi:10.1029/2012JC008021, URL https://agupubs.onlinelibrary.wiley.com/doi/abs/10.1029/2012JC008021, https://agupubs.onlinelibrary.wiley.com/doi/pdf/10.1029/2012JC008021.

Large, W. G., J. C. McWilliams, and S. C. Doney, 1994: Oceanic vertical mixing: A review and a model with a nonlocal boundary layer parameterization. *Reviews of Geophysics*, **32 (4)**, 363–403, doi:10.1029/94RG01872, URL https://agupubs.onlinelibrary.wiley.com/doi/abs/10.1029/94RG01872, https://agupubs.onlinelibrary.wiley.com/doi/pdf/10.1029/94RG01872.

Levitus, S., 1983: Climatological atlas of the world ocean. *Eos, Transactions American Geophysical Union*, **64 (49)**, 962–963, doi:10.1029/EO064i049p00962-02, URL https://agupubs.onlinelibrary.wiley.com/doi/abs/10.1029/EO064i049p00962-02, https://agupubs.onlinelibrary.wiley.com/doi/pdf/10.1029/EO064i049p00962-02.

Li, F., M. S. Lozier, G. Danabasoglu, N. P. Holliday, Y.-O. Kwon, A. Romanou, S. G. Yeager, and R. Zhang, 2019: Local and downstream relationships between labrador sea water volume and north atlantic meridional overturning circulation variability. *Journal of Climate*, **32 (13)**, 3883–3898, doi:10.1175/JCLI-D-18-0735.1, URL https://doi.org/10.1175/JCLI-D-18-0735.1, https://doi.org/10.1175/JCLI-D-18-0735.1.

Li, R. Z., D., and T. Knutson, 2017: On the discrepancy between observed and cmip5 multi-model simulated barents sea winter sea ice decline. *Nature Communications*, **8 (14991)**.

Lozier, M. M., S., and L. Jackson, 2020: Reconciling the role of the labrador sea overturning circulation in osnap and climate models.

Lozier, M. S., and Coauthors, 2019: A sea change in our view of overturning in the subpolar north atlantic. *Science*, **363 (6426)**, 516–521, doi:10.1126/science.aau6592, URL https://science.sciencemag.org/content/363/6426/516, https://science.sciencemag.org/content/363/6426/516.full.pdf.

MacMartin, D. G., E. Tziperman, and L. Zanna, 2013: Frequency domain multimodel analysis of the response of atlantic meridional overturning circulation to surface forcing. *Journal of Climate*, **26 (21)**, 8323–8340, doi:10.1175/JCLI-D-12-00717.1, URL https://doi.org/10.1175/JCLI-D-12-00717.1, https://doi.org/10.1175/JCLI-D-12-00717.1.

MacMartin, D. G., L. Zanna, and E. Tziperman, 2016: Suppression of atlantic meridional overturning circulation variability at increased co2. *Journal of Climate*, **29 (11)**, 4155–4164, doi:10.1175/JCLI-D-15-0533.1, URL https://doi.org/10.1175/JCLI-D-15-0533.1, https://doi.org/10.1175/JCLI-D-15-0533.1.

Mahajan, S., R. Zhang, and T. L. Delworth, 2011: Impact of the atlantic meridional overturning circulation (amoc) on arctic surface air temperature and sea ice variability. *Journal of Climate*, **24 (24)**, 6573–6581, doi:10.1175/2011JCLI4002.1, URL https://doi.org/10.1175/2011JCLI4002.1, https://doi.org/10.1175/2011JCLI4002.1.

Marsh, R., 2000: Recent variability of the north atlantic thermohaline circulation inferred from surface heat and freshwater fluxes. *Journal of Climate*, **13 (18)**, 3239–3260, doi:10.1175/1520-0442(2000)013<3239:RVOTNA>2.0.CO;2, URL https://doi.org/10.1175/1520-0442(2000)013<3239:RVOTNA>2.0.CO;2, https://doi.org/10.1175/1520-0442(2000)013<3239:RVOTNA>2.0.CO;2.

McCartney, M. S., and L. D. Talley, 1982: The subpolar mode water of the north atlantic ocean. *Journal of Physical Oceanography*, **12 (11)**, 1169–1188, doi:10.1175/1520-0485(1982)012<1169:TSMWOT>2.0.CO;2, URL https://doi.org/10.1175/1520-0485(1982)012<1169:TSMWOT>2.0.CO;2, https://doi.org/10.1175/1520-0485(1982)012<1169:TSMWOT>2.0.CO;2.

Mecking, J. V., N. S. Keenlyside, and R. J. Greatbatch, 2015: Multiple timescales of stochastically forced north atlantic ocean variability: A model study. *Ocean Dynamics*, **65 (9)**, 1367–1381, doi:10.1007/s10236-015-0868-0, URL https://doi.org/10.1007/s10236-015-0868-0.

Menary, M. B., D. L. R. Hodson, J. I. Robson, R. T. Sutton, and R. A. Wood, 2015a: A mechanism of internal decadal atlantic ocean variability in a high-resolution coupled climate model. *Journal* *of Climate*, **28 (19)**, 7764–7785, doi:10.1175/JCLI-D-15-0106.1, URL https://doi.org/10.1175/JCLI-D-15-0106.1, https://doi.org/10.1175/JCLI-D-15-0106.1.

Menary, M. B., D. L. R. Hodson, J. I. Robson, R. T. Sutton, R. A. Wood, and J. A. Hunt, 2015b: Exploring the impact of cmip5 model biases on the simulation of north atlantic decadal variability. *Geophysical Research Letters*, **42 (14)**, 5926–5934, doi:10.1002/2015GL064360, URL http://dx.doi.org/10.1002/2015GL064360, 2015GL064360.

Menary, M. B., L. Jackson, and S. Lozier, in review: Reconciling the role of the labrador sea in osnap and climate models. *Geophysical Research Letters*.

Menary, M. B., and Coauthors, 2018: Preindustrial control simulations with hadgem3-gc3.1 for cmip6. *Journal of Advances in Modeling Earth Systems*, **10 (12)**, 3049–3075, doi:10.1029/2018MS001495, URL https://agupubs.onlinelibrary.wiley.com/doi/abs/10.1029/2018MS001495, https://agupubs.onlinelibrary.wiley.com/doi/pdf/10.1029/2018MS001495.

Msadek, R., W. E. Johns, S. G. Yeager, G. Danabasoglu, T. L. Delworth, and A. Rosati, 2013: The atlantic meridional heat transport at 26.5°n and its relationship with the moc in the rapid array and the gfdl and ncar coupled models. *Journal of Climate*, **26 (12)**, 4335–4356, doi:10.1175/JCLI-D-12-00081.1, URL https://doi.org/10.1175/JCLI-D-12-00081.1, https://doi.org/10.1175/JCLI-D-12-00081.1.

Newsom, E. R., C. M. Bitz, F. O. Bryan, R. Abernathey, and P. R. Gent, 2016: Southern ocean deep circulation and heat uptake in a high-resolution climate model. *Journal of Climate*, **29 (7)**, 2597–2619, doi:10.1175/JCLI-D-15-0513.1, URL https://doi.org/10.1175/JCLI-D-15-0513.1, https://doi.org/10.1175/JCLI-D-15-0513.1.

Nurser, A. J. G., R. Marsh, and R. G. Williams, 1999: Diagnosing water mass formation from air–sea fluxes and surface mixing. *Journal of Physical Oceanography*, **29 (7)**, 1468–1487, doi:10.1175/1520-0485(1999)029<1468:DWMFFA>2.0.CO;2, URL https://doi.org/10.1175/1520-0485(1999)029<1468:DWMFFA>2.0.CO;2, https://doi.org/10.1175/1520-0485(1999)029<1468:DWMFFA>2.0.CO;2.

Oldenburg, D., K. C. Armour, L. Thompson, and C. M. Bitz, 2018: Distinct mechanisms of ocean heat transport into the arctic under internal variability and climate change. *Geophysical Research Letters*, **45 (15)**, 7692–7700, doi:10.1029/2018GL078719, URL https://agupubs.onlinelibrary.wiley.com/doi/abs/10.1029/2018GL078719, https://agupubs.onlinelibrary.wiley.com/doi/pdf/10.1029/2018GL078719.

Peixoto, J. P., and A. H. Oort, 1993: Physics of climate. *American Institute of Physics, New York*, 520.

Pérez-Brunius, P., T. Rossby, and D. R. Watts, 2004: Transformation of the warm waters of the north atlantic from a geostrophic streamfunction perspective. *Journal of Physical Oceanography*, **34 (10)**, 2238–2256, doi:10.1175/1520-0485(2004)034<2238:TOTWWO>2.0.CO;2, URL https://doi.org/10.1175/1520-0485(2004)034<2238:TOTWWO>2.0.CO;2, https://doi.org/10.1175/1520-0485(2004)034<2238:TOTWWO>2.0.CO;2.

Pickart, R. S., and M. A. Spall, 2007: Impact of labrador sea convection on the north atlantic meridional overturning circulation. *Journal of Physical Oceanography*, **37 (9)**, 2207–2227, doi:10.1175/JPO3178.1, URL https://doi.org/10.1175/JPO3178.1, https://doi.org/10.1175/JPO3178.1.

Reynolds, R. W., N. A. Rayner, T. M. Smith, D. C. Stokes, and W. Wang, 2002: An improved in situ and satellite sst analysis for climate. *Journal of Climate*, **15 (13)**, 1609–1625, doi:10.1175/

1520-0442(2002)015<1609:AIISAS>2.0.CO;2, URL https://doi.org/10.1175/1520-0442(2002)015<1609:AIISAS>2.0.CO;2, https://doi.org/10.1175/1520-0442(2002)015<1609:AIISAS>2.0.CO;2.

Roberts, M. J., and Coauthors, 2019: Description of the resolution hierarchy of the global coupled hadgem3-gc3.1 model as used in cmip6 highresmip experiments. *Geoscientific Model Development*, **12 (12)**, 4999–5028, doi:10.5194/gmd-12-4999-2019, URL https://www.geosci-model-dev.net/12/4999/2019/.

Roberts, M. J., and Coauthors, 2020: Sensitivity of the atlantic meridional overturning circulation to model resolution in cmip6 highresmip simulations and implications for future changes. *Journal of Advances in Modeling Earth Systems*, doi:10.1029/2019MS002014, URL https://agupubs.onlinelibrary.wiley.com/doi/abs/10.1029/2019MS002014, e2019MS002014 2019MS002014, https://agupubs.onlinelibrary.wiley.com/doi/pdf/10.1029/2019MS002014.

Schlesinger, M. E., and N. Ramankutty, 1994: An oscillation in the global climate system of period 65–70 years. *Nature*, **367 (6465)**, 723–726, doi:10.1038/367723a0, URL https://doi.org/10.1038/367723a0.

Schneider, T., and S. Griffies, 1999: A conceptual framework for predictability studies. *Journal of Climate*, **12**, 3133–3155, doi:10.1175/1520-0442(1999)012<3133:ACFFPS>2.0.CO;2.

Schneider, T., and I. M. Held, 2001: Discriminants of twentieth-century changes in earth surface temperatures. *Journal of Climate*, **14 (3)**, 249–254, doi:10.1175/1520-0442(2001)014<0249:LDOTCC>2.0.CO;2, URL https://doi.org/10.1175/1520-0442(2001)014<0249:LDOTCC>2.0.CO;2, https://doi.org/10.1175/1520-0442(2001)014<0249:LDOTCC>2.0.CO;2.

Speer, K., and E. Tziperman, 1992: Rates of water mass formation in the north atlantic ocean. *Journal of Physical Oceanography*, **22 (1)**, 93–104, doi:10.1175/1520-0485(1992)022<0093:ROWMFI>2.0.CO;2, URL https://doi.org/10.1175/1520-0485(1992)022<0093:ROWMFI>2.0.CO;2, https://doi.org/10.1175/1520-0485(1992)022<0093:ROWMFI>2.0.CO;2.

Straneo, F., 2006a: Heat and freshwater transport through the central labrador sea. *Journal of Physical Oceanography*, **36 (4)**, 606–628, doi:10.1175/JPO2875.1, URL https://doi.org/10.1175/JPO2875.1, https://doi.org/10.1175/JPO2875.1.

Straneo, F., 2006b: On the connection between dense water formation, overturning, and poleward heat transport in a convective basin. *Journal of Physical Oceanography*, **36 (9)**, 1822–1840, doi:10.1175/JPO2932.1, URL https://doi.org/10.1175/JPO2932.1, https://doi.org/10.1175/JPO2932.1.

Talley, L. D., J. L. Reid, and P. E. Robbins, 2003: Data-based meridional overturning streamfunctions for the global ocean. *Journal of Climate*, **16 (19)**, 3213–3226, doi:10.1175/1520-0442(2003)016<3213:DMOSFT>2.0.CO;2, URL https://doi.org/10.1175/1520-0442(2003)016<3213:DMOSFT>2.0.CO;2, https://doi.org/10.1175/1520-0442(2003)016<3213:DMOSFT>2.0.CO;2.

Tandon, A., and L. Zhao, 2004: Mixed layer transformation for the north atlantic for 1990–2000. *Journal of Geophysical Research: Oceans*, **109 (C5)**, doi:10.1029/2003JC002059, URL https://agupubs.onlinelibrary.wiley.com/doi/abs/10.1029/2003JC002059, https://agupubs.onlinelibrary.wiley.com/doi/pdf/10.1029/2003JC002059.

Taylor, K. E., R. J. Stouffer, and G. A. Meehl, 2012: An overview of cmip5 and the experiment design. *Bulletin of the American Meteorological Society*, **93 (4)**, 485–498, doi:10.1175/BAMS-D-11-00094.1, URL https://doi.org/10.1175/BAMS-D-11-00094.1, https://doi.org/10.1175/BAMS-D-11-00094.1.

Ting, M., Y. Kushnir, R. Seager, and C. Li, 2009: Forced and internal twentieth-century sst trends in the north atlantic. *Journal of Climate*, **22 (6)**, 1469–1481, doi:10.1175/2008JCLI2561.1, URL https://doi.org/10.1175/2008JCLI2561.1, https://doi.org/10.1175/2008JCLI2561.1.

Treguier, A. M., S. Theetten, E. P. Chassignet, T. Penduff, R. Smith, L. Talley, J. O. Beismann, and C. Böning, 2005: The north atlantic subpolar gyre in four high-resolution models. *Journal of Physical Oceanography*, **35 (5)**, 757–774, doi:10.1175/JPO2720.1, URL https://doi.org/10.1175/JPO2720.1, https://doi.org/10.1175/JPO2720.1.

Tulloch, R., and J. Marshall, 2012: Exploring mechanisms of variability and predictability of atlantic meridional overturning circulation in two coupled climate models. *Journal of Climate*, **25 (12)**, 4067–4080, doi:10.1175/JCLI-D-11-00460.1, URL https://doi.org/10.1175/JCLI-D-11-00460.1, https://doi.org/10.1175/JCLI-D-11-00460.1.

Tziperman, E., 1986: On the role of interior mixing and air-sea fluxes in determining the stratification and circulation of the oceans. *Journal of Physical Oceanography*, **16 (4)**, 680–693, doi:10.1175/1520-0485(1986)016<0680:OTROIM>2.0.CO;2, URL https://doi.org/10.1175/1520-0485(1986)016<0680:OTROIM>2.0.CO;2, https://doi.org/10.1175/1520-0485(1986)016<0680:OTROIM>2.0.CO;2.

Venzke, S., M. R. Allen, R. T. Sutton, and D. P. Rowell, 1999: The atmospheric response over the north atlantic to decadal changes in sea surface temperature. *Journal of Climate*, **12 (8)**, 2562–2584, doi:10.1175/1520-0442(1999)012<2562:TAROTN>2.0.CO;2, URL https://doi.org/10.1175/1520-0442(1999)012<2562:TAROTN>2.0.CO;2, https://doi.org/10.1175/1520-0442(1999)012<2562:TAROTN>2.0.CO;2.

Vörösmarty, C., B. Fekete, M. Meybeck, and R. Lammers, 2000: Geomorphometric attributes of the global system of rivers at 30-minute spatial resolution. *Journal of Hydrology*, **237 (1)**, 17 – 39, doi:https://doi.org/10.1016/S0022-1694(00)00282-1, URL http://www.sciencedirect.com/science/article/pii/S0022169400002821.

Walin, G., 1982: On the relation between sea-surface heat flow and thermal circulation in the ocean. *Tellus*, **34 (2)**, 187–195, doi:10.1111/j.2153-3490.1982.tb01806.x, URL https://onlinelibrary.wiley.com/doi/abs/10.1111/j.2153-3490.1982.tb01806.x, https://onlinelibrary.wiley.com/doi/pdf/10.1111/j.2153-3490.1982.tb01806.x.

Wills, R. C., and T. Schneider, 2015: Stationary eddies and the zonal asymmetry of net precipitation and ocean freshwater forcing. *Journal of Climate*, **28 (13)**, 5115–5133, doi:10.1175/JCLI-D-14-00573.1, URL https://doi.org/10.1175/JCLI-D-14-00573.1, https://doi.org/10.1175/JCLI-D-14-00573.1.

Wills, R. C., T. Schneider, J. M. Wallace, D. S. Battisti, and D. L. Hartmann, 2018: Disentangling global warming, multidecadal variability, and el niño in pacific temperatures. *Geophysical Research Letters*, **45 (5)**, 2487–2496, doi:10.1002/2017GL076327, URL https://agupubs.onlinelibrary.wiley.com/doi/abs/10.1002/2017GL076327, https://agupubs.onlinelibrary.wiley.com/doi/pdf/10.1002/2017GL076327.

Wills, R. C. J., K. C. Armour, D. S. Battisti, and D. L. Hartmann, 2019a: Ocean–atmosphere dynamical coupling fundamental to the atlantic multidecadal oscillation. *Journal of Climate*, **32 (1)**, 251–272, doi:10.1175/JCLI-D-18-0269.1, URL https://doi.org/10.1175/JCLI-D-18-0269.1, https://doi.org/10.1175/JCLI-D-18-0269.1.

Wills, R. C. J., D. S. Battisti, C. Proistosescu, L. Thompson, D. L. Hartmann, and K. C. Armour, 2019b: Ocean circulation signatures of north pacific decadal variability. *Geophysi-*

cal Research Letters, **46 (3)**, 1690–1701, doi:10.1029/2018GL080716, URL https://agupubs.onlinelibrary.wiley.com/doi/abs/10.1029/2018GL080716, https://agupubs.onlinelibrary.wiley.com/doi/pdf/10.1029/2018GL080716.

Yan, X., R. Zhang, and T. R. Knutson, 2018: Underestimated amoc variability and implications for amv and predictability in cmip models. *Geophysical Research Letters*, **45 (9)**, 4319–4328, doi:10.1029/2018GL077378, URL https://agupubs.onlinelibrary.wiley.com/doi/abs/10.1029/2018GL077378, https://agupubs.onlinelibrary.wiley.com/doi/pdf/10.1029/2018GL077378.

Yeager, S. G., A. R. Karspeck, and G. Danabasoglu, 2015: Predicted slowdown in the rate of atlantic sea ice loss. *Geophysical Research Letters*, **42 (24)**, 10,704–10,713, doi:10.1002/2015GL065364, URL http://dx.doi.org/10.1002/2015GL065364, 2015GL065364.

Yu, X. J., L., and R. A. Weller, 2008: Multidecade global flux datasets from the objectively analyzed air-sea fluxes (oaflux) project: Latent and sensible heat fluxes, ocean evaporation, and related surface meteorological variables. *OAFlux Project Technical Report*, **OA-2008-01**.

Zhang, L., and C. Wang, 2013: Multidecadal north atlantic sea surface temperature and atlantic meridional overturning circulation variability in cmip5 historical simulations. *Journal of Geophysical Research: Oceans*, **118 (10)**, 5772–5791, doi:10.1002/jgrc.20390, URL https://agupubs.onlinelibrary.wiley.com/doi/abs/10.1002/jgrc.20390, https://agupubs.onlinelibrary.wiley.com/doi/pdf/10.1002/jgrc.20390.

Zhang, R., 2010: Latitudinal dependence of atlantic meridional overturning circulation (amoc) variations. *Geophysical Research Letters*, **37 (16)**, doi:10.1029/2010GL044474, URL https://agupubs.onlinelibrary.wiley.com/doi/abs/10.1029/2010GL044474, https://agupubs.onlinelibrary.wiley.com/doi/pdf/10.1029/2010GL044474.

Zhang, R., 2015: Mechanisms for low-frequency variability of summer arctic sea ice extent. *Proceedings of the National Academy of Sciences*, **112 (15)**, 4570–4575, doi:10.1073/pnas.1422296112, URL http://www.pnas.org/content/112/15/4570.abstract, http://www.pnas.org/content/112/15/4570.full.pdf.

Zou, S., M. S. Lozier, F. Li, R. Abernathey, and L. Jackson, 2020: Density-compensated overturning in the labrador sea. *Nature Geoscience*, doi:10.1038/s41561-019-0517-1, URL https://doi.org/10.1038/s41561-019-0517-1.

LIST OF FIGURES

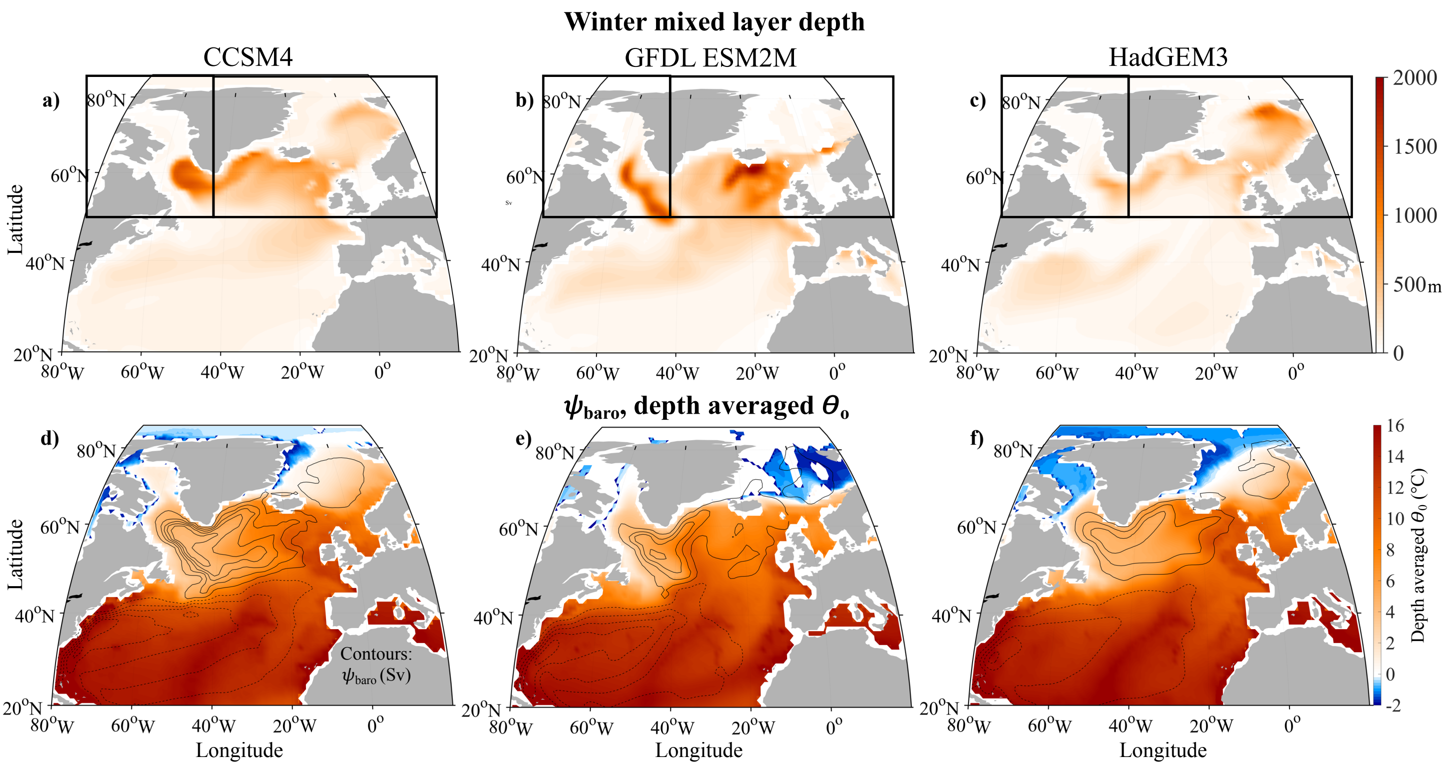

Fig. 1. Climatological fields in CCSM4 (left column), GFDL ESM2M (middle column) and HadGEM3 (right column). **a**, **b**, **c)** Mixed layer depth averaged over January, February and March. Left boxes define the area of integration in the Labrador Sea in our calculations, right boxes indicate the area of integration for the GIN Seas. **d**, **e**, **f)** Contours show the barotropic streamfunction, spaced every 10 Sv, where solid lines indicate cyclonic/positive values, and dashed lines indicate anticyclonic/negative values. Colors show the depth-averaged potential temperature.

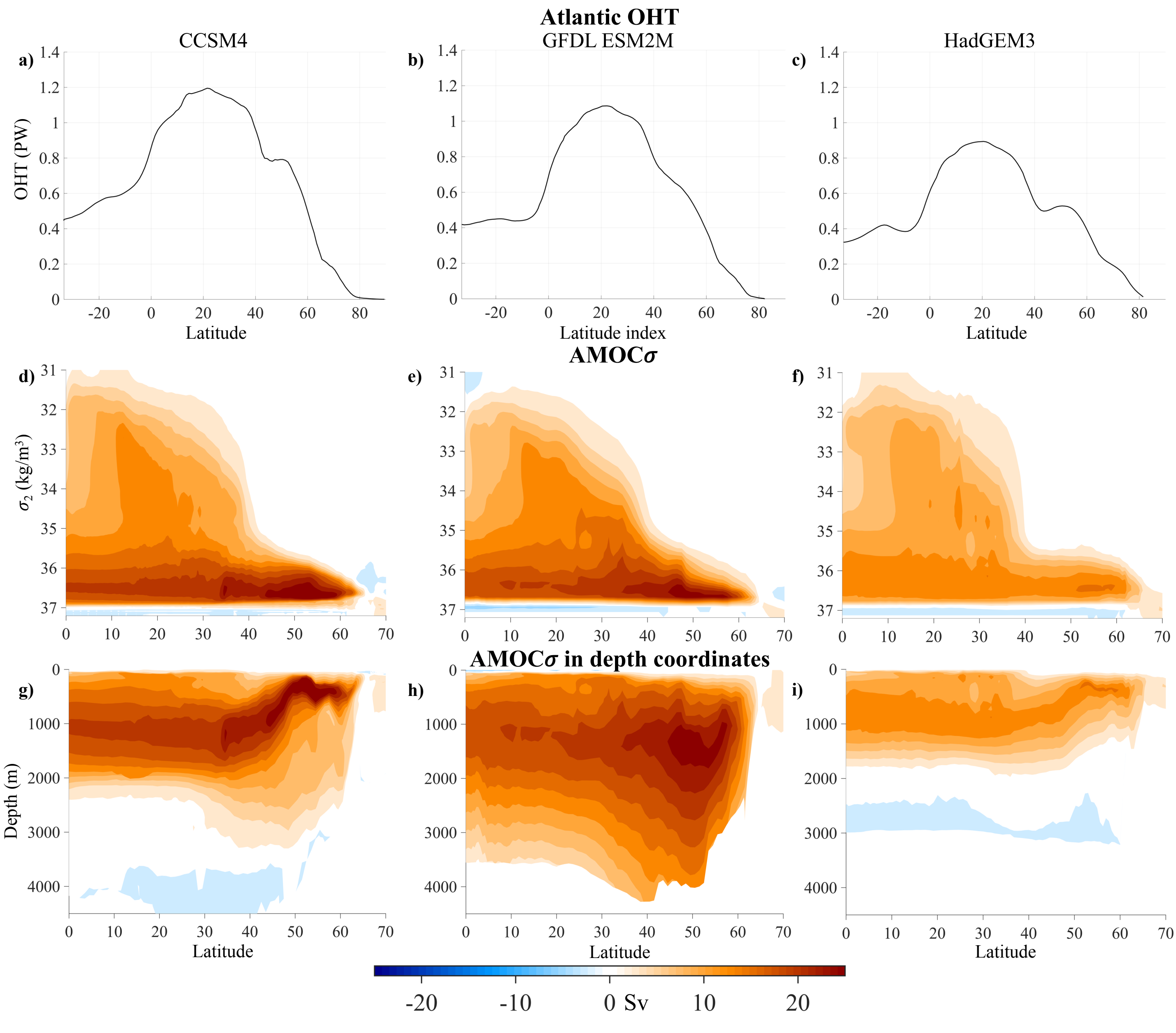

1061 Fig. 2. Climatological fields in CCSM4 (left column), GFDL ESM2M (middle column) and HadGEM3 (right
1062 column). **a**, **b**, **c)** Atlantic OHT. **d**, **e**, **f)** AMOCσ. **g**, **h**, **i)** AMOCσ remapped to depth coordinates.

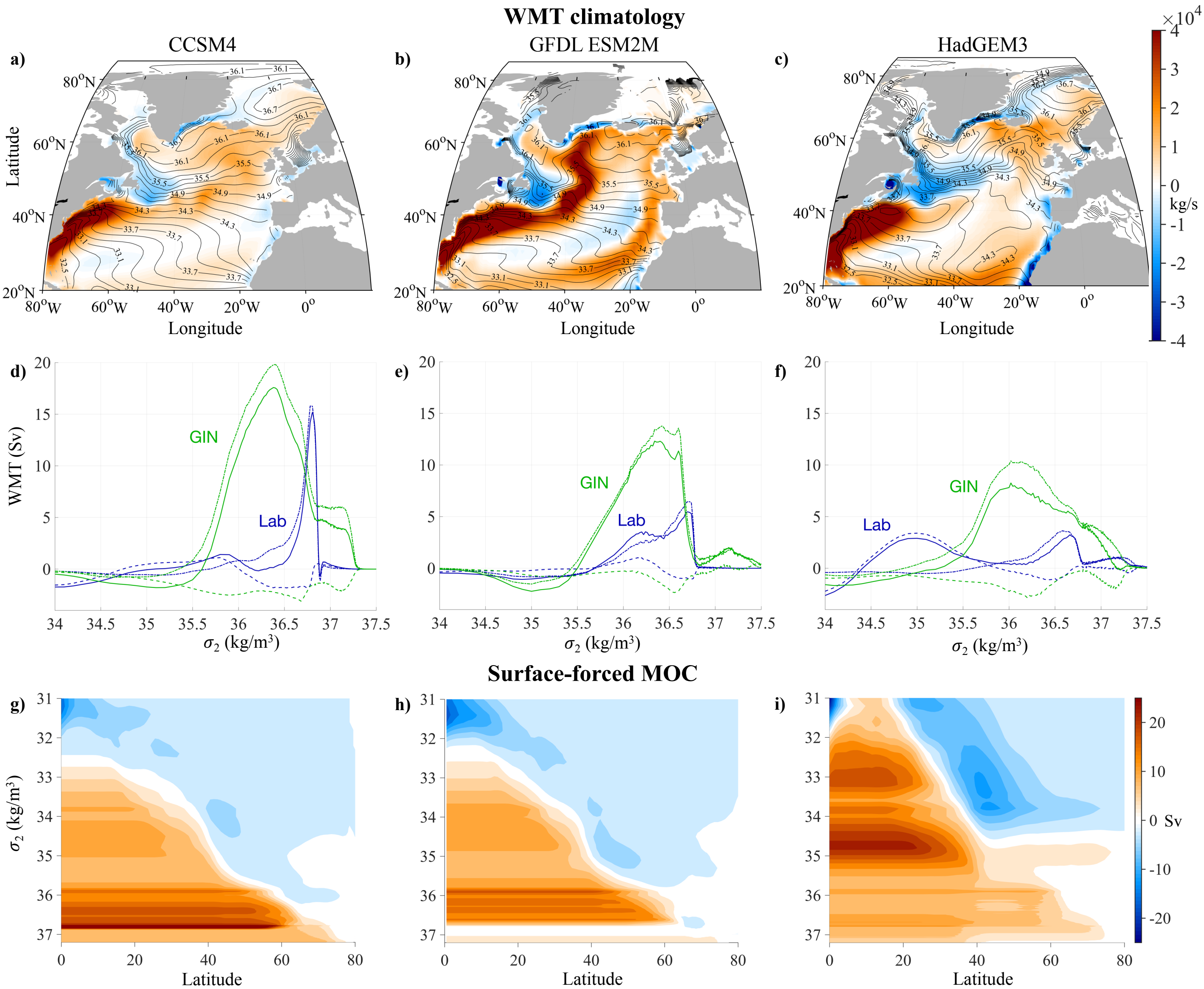

Fig. 3. Climatological fields in CCSM4 (left column), GFDL ESM2M (middle column) and HadGEM3 (right column). **a**, **b**, **c)** Total water mass transformation as a function of latitude and longitude. **d**, **e**, **f)** Water mass transformation thermal (dot-dash lines), freshwater (dashed lines) and total (solid lines) components in the Labrador Sea and GIN Seas. **g**, **h**, **i)** Surface-forced overturning streamfunction in density coordinates.

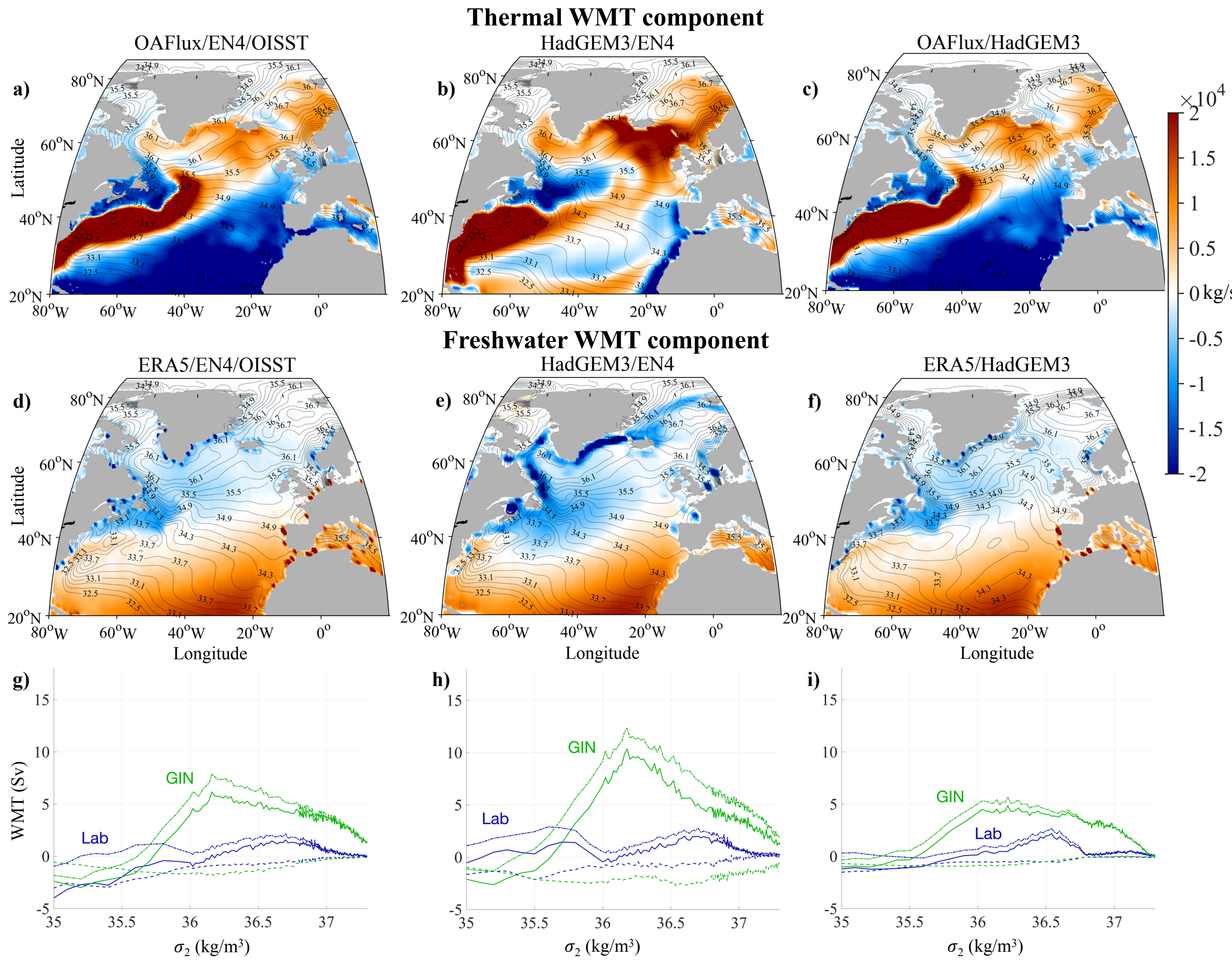

FIG. 4. Water-mass transformation computed from observations and model fields. **a**, **b**, **c)** Thermal component of water mass transformation (WMT) as a function of longitude and latitude calculated using **a)** OAFlux surface heat fluxes convolved with OISST SSTs and EN4.2.1 surface salinities, **b)** HadGEM3 heat fluxes convolved with OISST SSTs and EN4.2.1 surface salinities, **c)** OAFlux heat fluxes convolved with HadGEM3 SSTs and surface salinities. Middle row: Freshwater component of WMT calculated using **d)** ERA5 surface freshwater fluxes convolved with OISST SSTs and EN4.2.1 surface salinities, **e)** HadGEM3 freshwater fluxes convolved with OISST SSTs and EN4.2.1 surface salinities, **f)** ERA5 freshwater fluxes convolved with HadGEM3 SSTs and surface salinities. In the top and middle rows, black contours show sea-surface potential density based on the relevant model or observational dataset. Bottom row: WMT thermal (dot-dash lines), freshwater (dashed lines) and total (solid lines) components integrated over the Labrador Sea and GIN Seas boxes calculated using **g)** OAFlux surface heat fluxes and ERA5 freshwater fluxes convolved with OISST SSTs and EN4.2.1 surface salinities, **h)** HadGEM3 heat and freshwater fluxes convolved with OISST SSTs and EN4.2.1 surface salinities, **i)** OAFlux heat fluxes and ERA5 freshwater fluxes convolved with HadGEM3 SSTs and surface salinities.

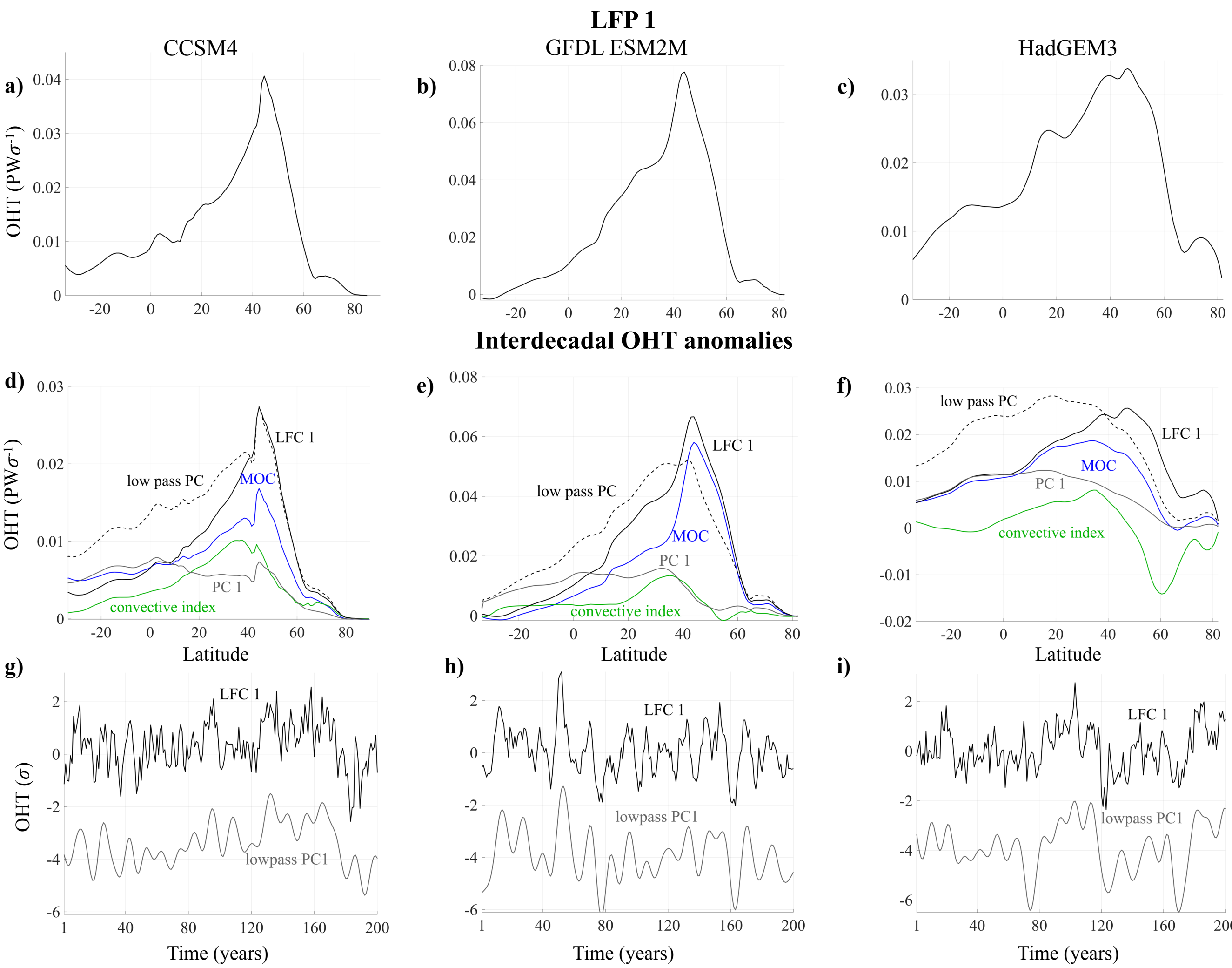

Fig. 5. Top row: First LFP of Atlantic OHT for **a)** CCSM4, **b)** GFDL ESM2M and **c)** HadGEM3. Middle row: Regressions of 10-year low-pass filtered Atlantic OHT on different indices for **d)** CCSM4, **e)** GFDL ESM2M and **f)** HadGEM3. The AMOC index is the normalised maximum value of the meridional overturning streamfunction in depth coordinates across all depths and latitudes north of 30°N. The convective index is the normalised density anomaly in the models' respective convective regions, excluding grid cells with winter MLD < 500m for CCSM4, winter MLD < 700m for GFDL ESM2M and winter MLD < 400m for HadGEM3. PC1 represents the first principal component of the OHT. Lowpass PC1 is the first principal component of the 10 year low pass filtered OHT. Bottom row: Time series for both LFC 1 and the lowpass PC1 for **g)** CCSM4, **h)** GFDL ESM2M and **i)** HadGEM3. Lowpass PC1 time series are shifted downwards by −4 on the y-axis.

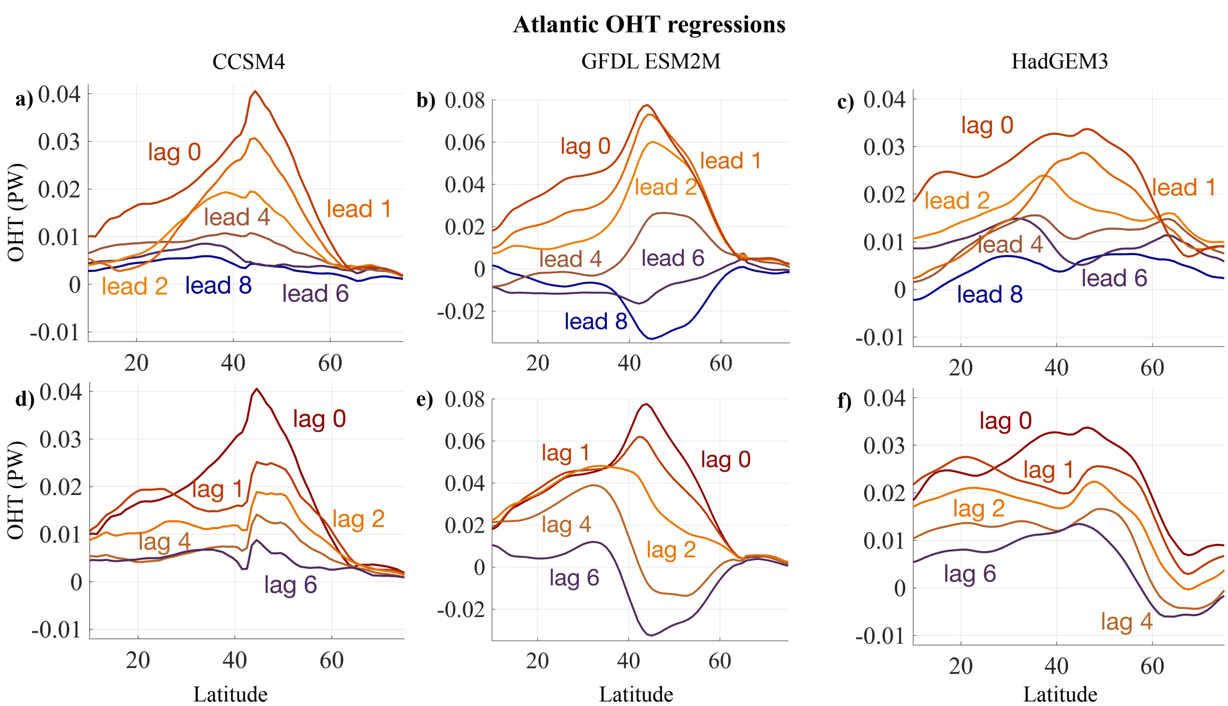

FIG. 6. Lead-lag regressions of OHT onto the first LFC of OHT for CCSM4 (left column), GFDL ESM2M (middle column) and HadGEM3 (right column). Lead means LFC 1 lags, i.e., prior to the maximum OHT. **a**, **b**, **c)** Lead times. **d**, **e**, **f)** Lag times.

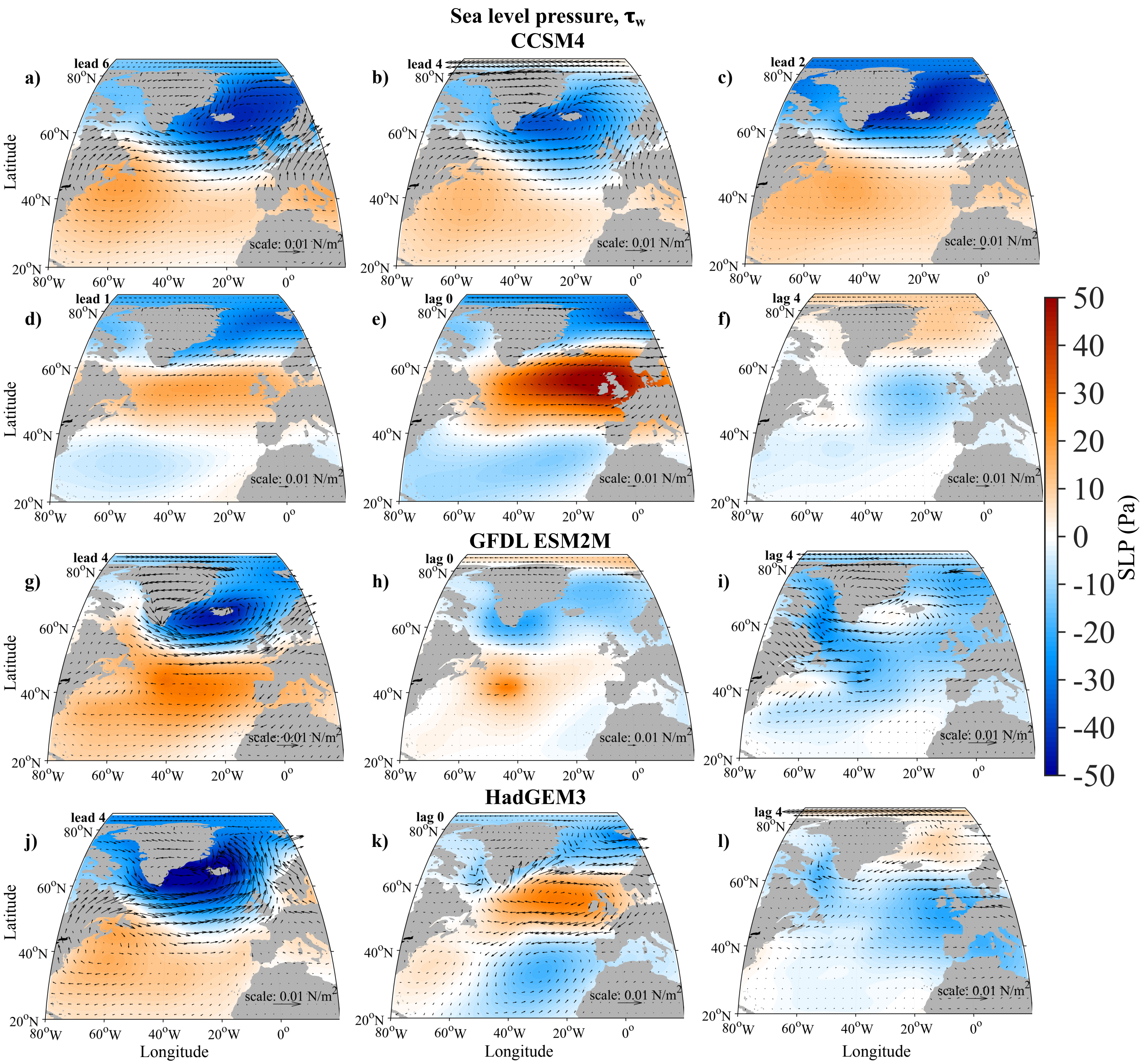

1092 FIG. 7. Lead-lag regressions of sea level pressure (colors) and surface wind stress (arrows) onto the first LFC
1093 of OHT for **(a-f)** CCSM4, **(g-i)** GFDL ESM2M and **(j-l)** HadGEM3. Lead times represent times when the LFC
1094 lags, i.e., prior to the maximum OHT.

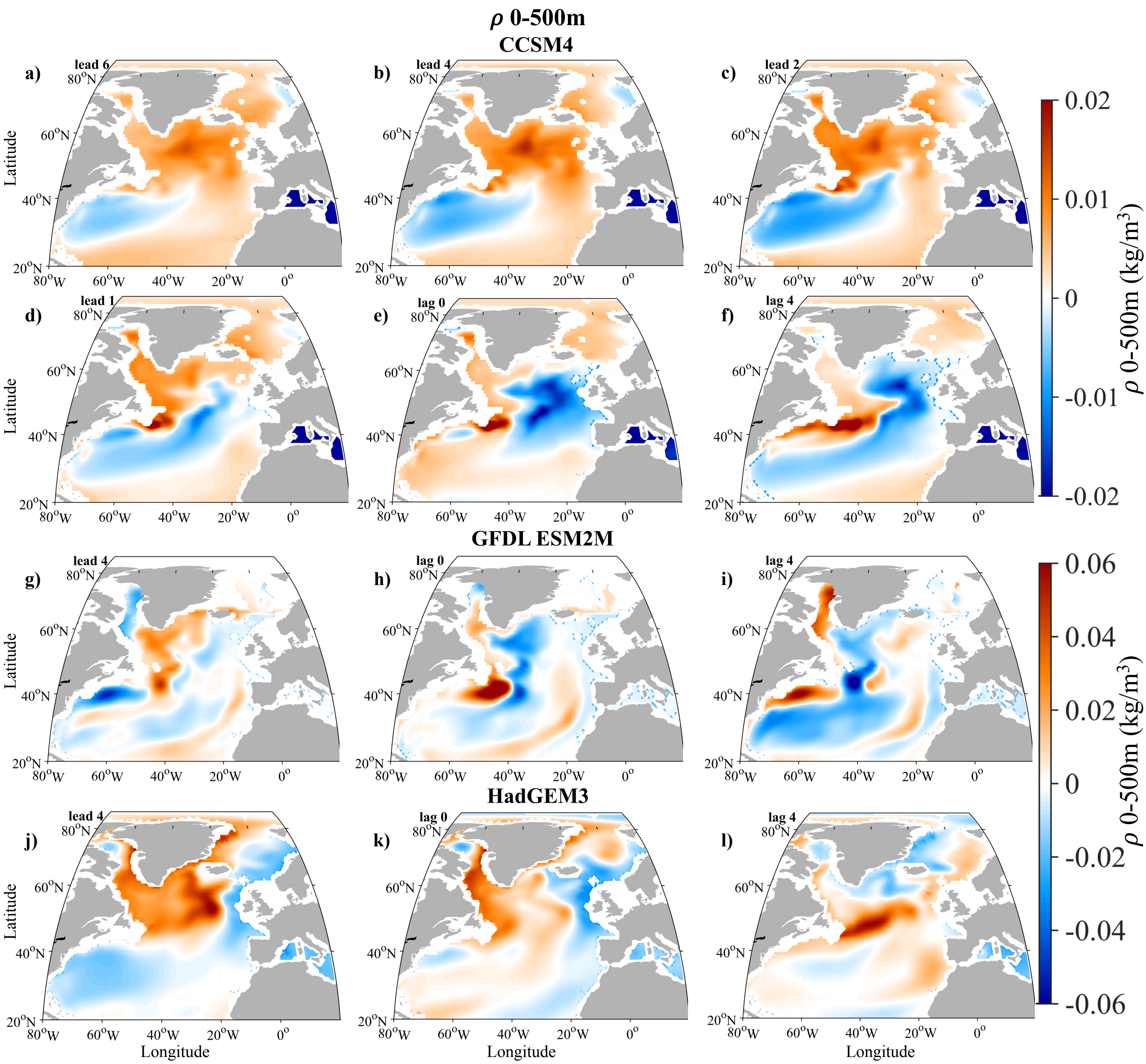

1095 FIG. 8. Lead-lag regressions of water density averaged over 0-500 m onto the first LFC of OHT for **(a-f)** CCSM4, **(g-i)** GFDL ESM2M and **(j-l)** HadGEM3. Lead times represent times when the LFC lags, i.e., prior to the maximum OHT.

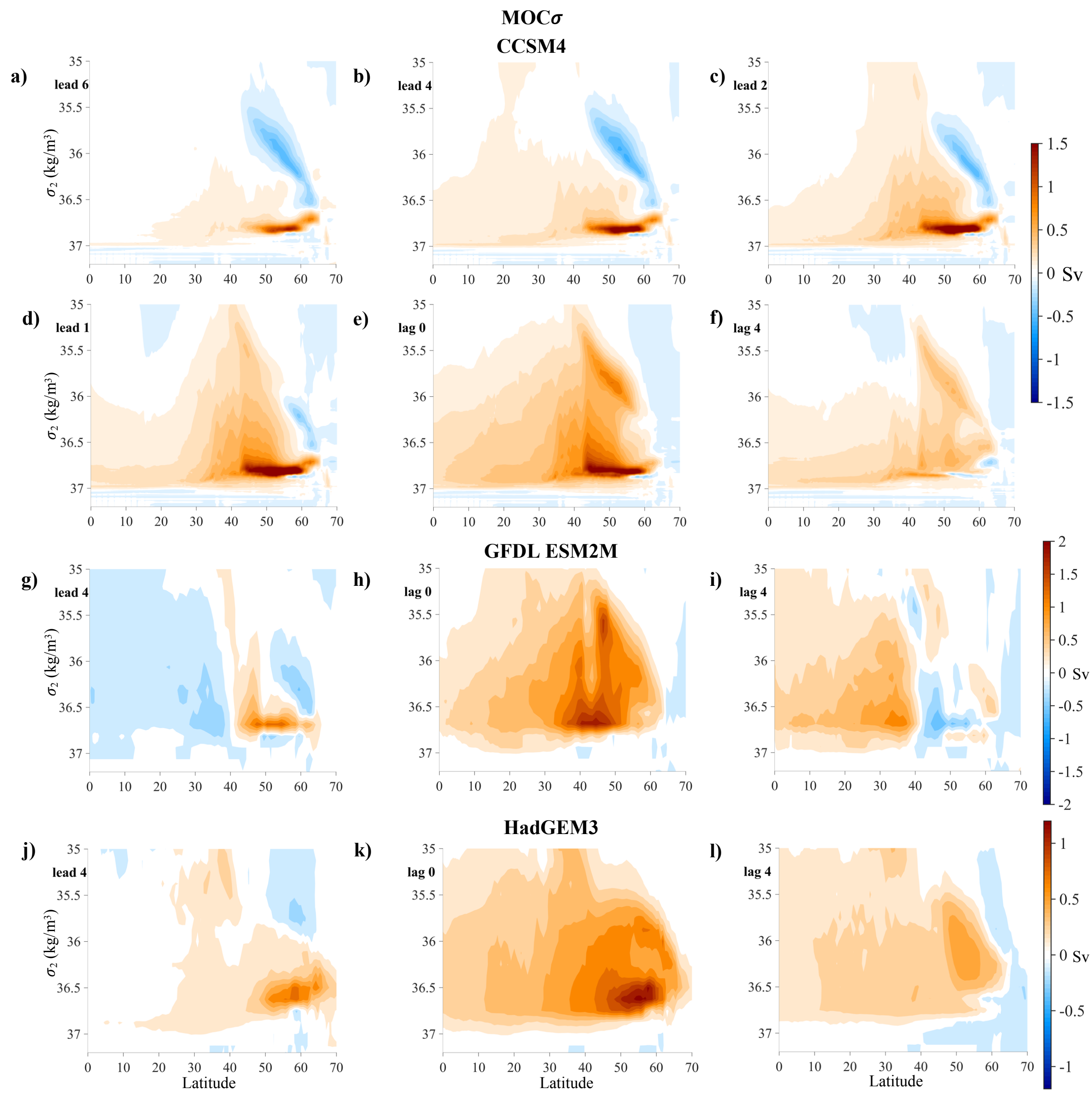

FIG. 9. Lead-lag regressions of the overturning streamfunction onto the first LFC of OHT for **(a-f)** CCSM4, **(g-i)** GFDL ESM2M and **(j-l)** HadGEM3. Lead times represent times when the LFC lags, i.e., prior to the maximum OHT.

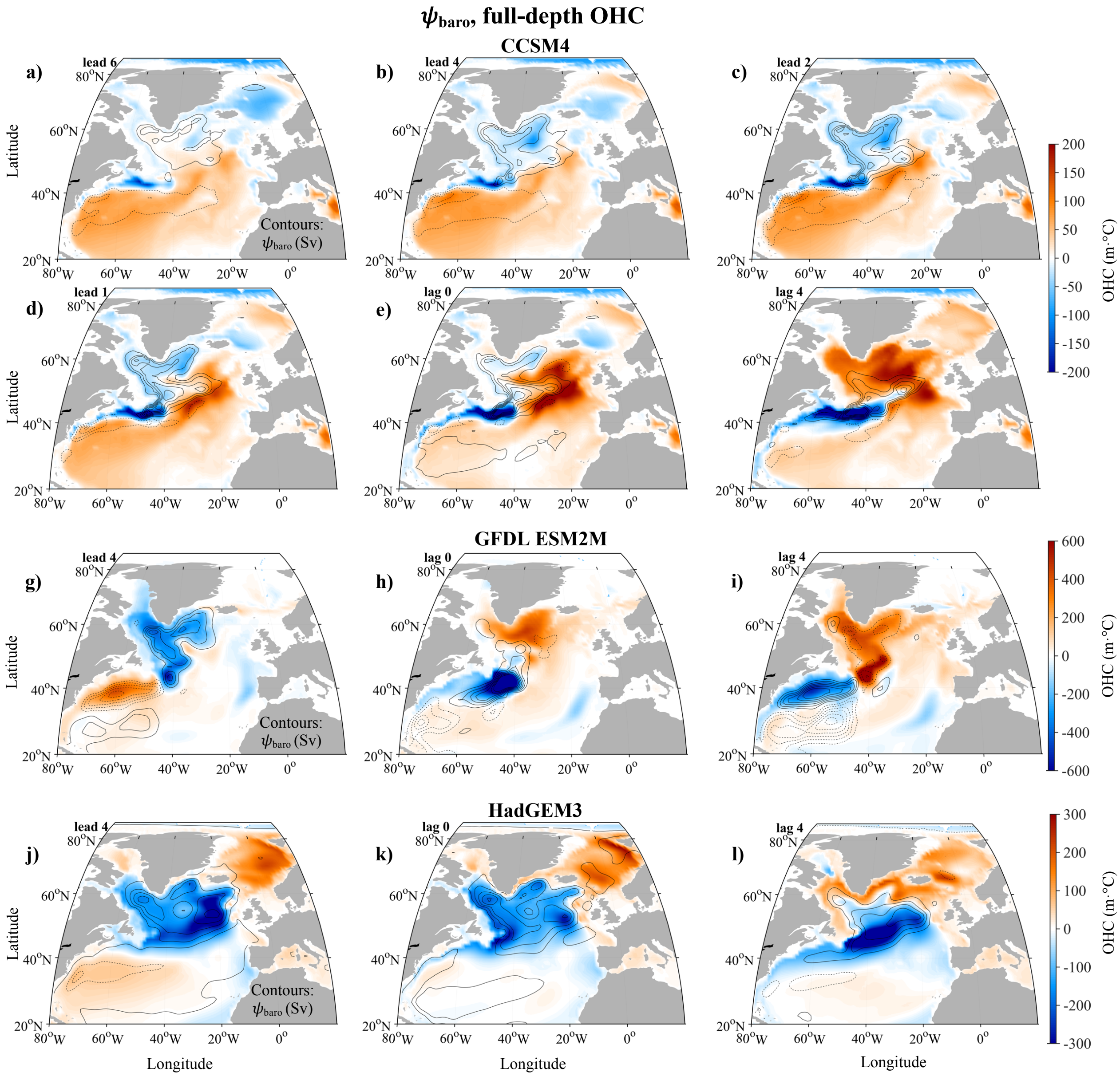

Fig. 10. Lead-lag regressions of the barotropic streamfunction (contours) and full-depth ocean heat content (colors) onto the first LFC of OHT for **(a-f)** CCSM4, **(g-i)** GFDL ESM2M and **(j-l)** HadGEM3. Barotropic streamfunction contours are spaced every 0.25 Sv for CCSM4 and HadGEM3 and 0.5 Sv for GFDL ESM2M. Solid lines indicate cyclonic/positive values, and dashed lines indicate anticyclonic/negative values. Lead times represent times when the LFC lags, i.e., prior to the maximum OHT.

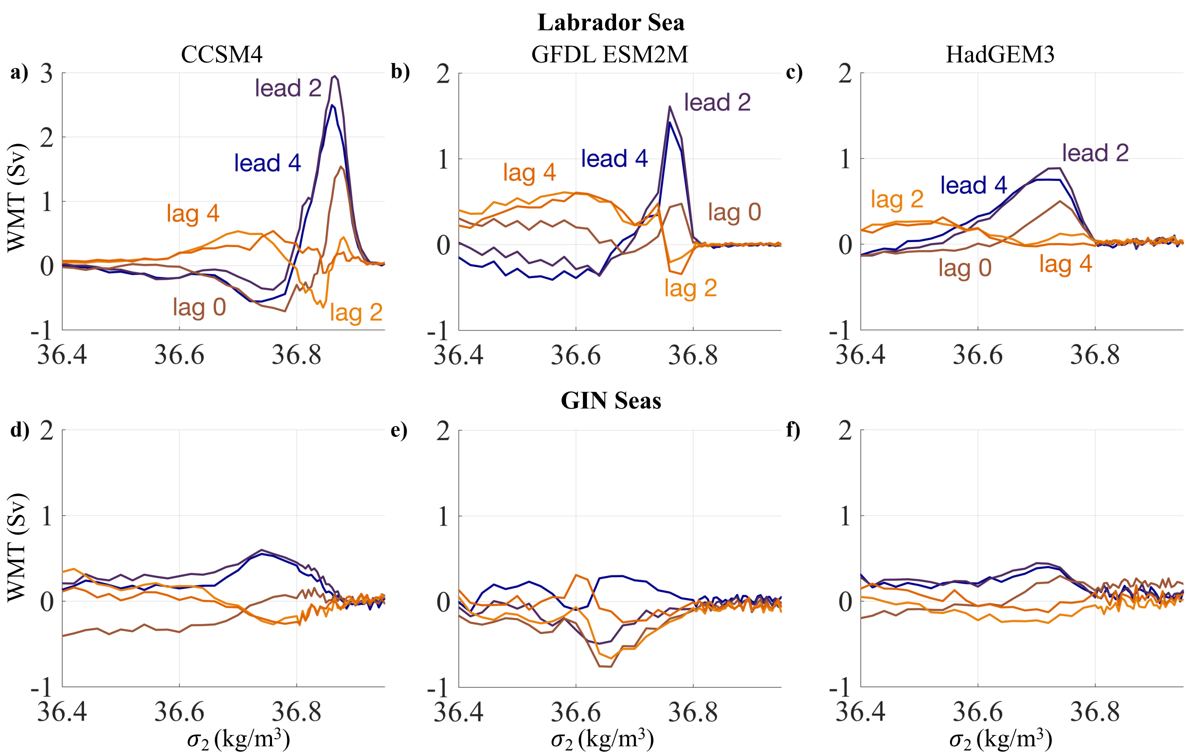

FIG. 11. Lead-lag regressions of water mass transformation (WMT) onto the first LFC of OHT for CCSM4 (left column), GFDL ESM2M (middle column) and HadGEM3 (right column). **a, b, c)** WMT summed over the Labrador Sea region. **d, e, f)** WMT summed over the Greenland-Iceland-Norwegian (GIN) Seas. The left and right boxes in Fig. 1 **a, b, c)** represent what we consider to be the Labrador Sea and GIN Seas in this calculation. Lead means LFC 1 lags, i.e., prior to the maximum OHT.

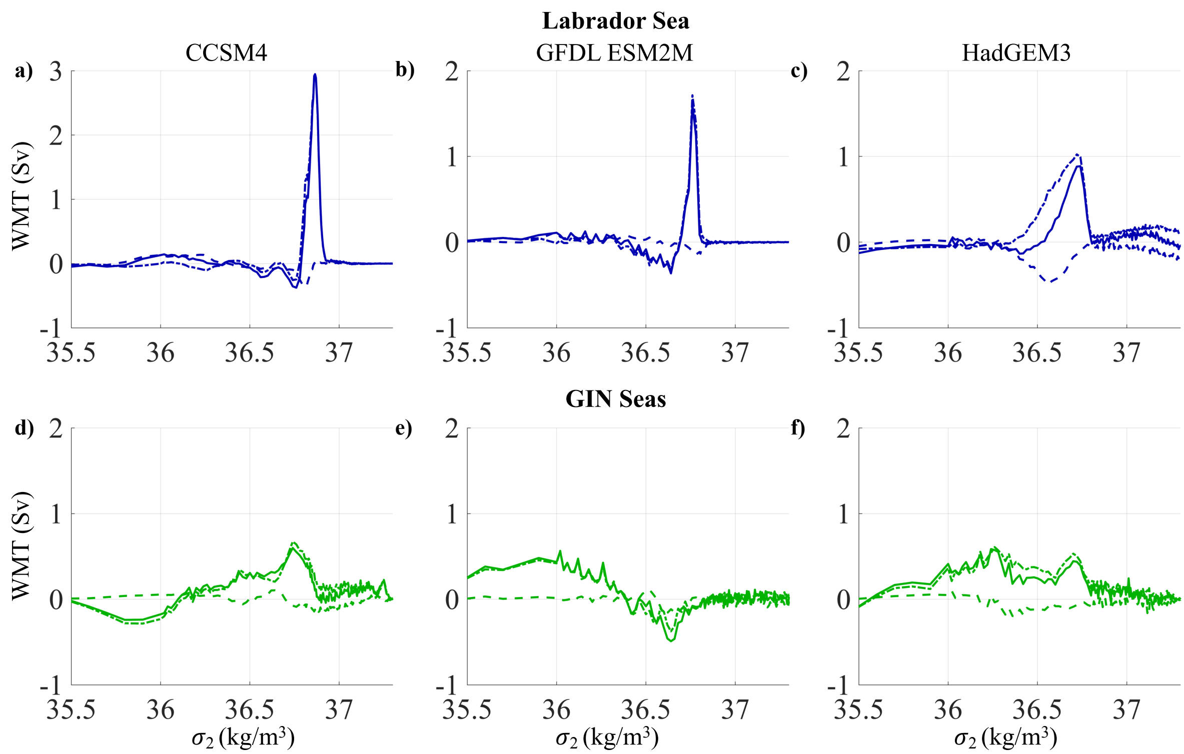

FIG. 12. 2-year lead-time regressions of thermal (dot-dash lines), freshwater (dashed lines) and total (solid lines) WMT components onto the first LFC of OHT for CCSM4 (left column), GFDL ESM2M (middle column) and HadGEM3 (right column). **a, b, c)** WMT summed over the Labrador Sea region. **d, e, f)** WMT summed over the Greenland-Iceland-Norwegian (GIN) Seas. The left and right boxes in Fig. 1 **a, b, c)** represent what we consider to be the Labrador Sea and GIN Seas in this calculation.